



UNIVERSITY OF LEEDS

This is a repository copy of *Observational Evidence of Increasing Global Radiative Forcing*.

White Rose Research Online URL for this paper:
<https://eprints.whiterose.ac.uk/174407/>

Version: Accepted Version

Article:

Kramer, RJ, He, H, Soden, BJ et al. (4 more authors) (2021) Observational Evidence of Increasing Global Radiative Forcing. *Geophysical Research Letters*, 48 (7). ISSN 0094-8276

<https://doi.org/10.1029/2020gl091585>

© 2021. American Geophysical Union. All Rights Reserved. This is the peer reviewed version of the following article: Kramer, RJ, He, H, Soden, BJ et al. (4 more authors) (2021) Observational Evidence of Increasing Global Radiative Forcing. *Geophysical Research Letters*, 48 (7). ISSN 0094-8276, which has been published in final form at *Geophysical Research Letters*. This article may be used for non-commercial purposes in accordance with Wiley Terms and Conditions for Use of Self-Archived Versions.

Reuse

Items deposited in White Rose Research Online are protected by copyright, with all rights reserved unless indicated otherwise. They may be downloaded and/or printed for private study, or other acts as permitted by national copyright laws. The publisher or other rights holders may allow further reproduction and re-use of the full text version. This is indicated by the licence information on the White Rose Research Online record for the item.

Takedown

If you consider content in White Rose Research Online to be in breach of UK law, please notify us by emailing eprints@whiterose.ac.uk including the URL of the record and the reason for the withdrawal request.



eprints@whiterose.ac.uk
<https://eprints.whiterose.ac.uk/>

1 Observational evidence of increasing global radiative forcing

2
3 Ryan J. Kramer^{1,2,*}, Haozhe He³, Brian J. Soden³, Lazaros Oreopoulos¹, Gunnar Myhre⁴,
4 Piers M. Forster⁵, Christopher J. Smith^{5,6}
5
6

7 ¹Earth Sciences Division, NASA Goddard Space Flight Center, Greenbelt, MD 20771, USA

8 ²Universities Space Research Association, 7178 Columbia Gateway Drive, Columbia, MD
9 21046, USA

10 ³Rosenstiel School of Marine and Atmospheric Science, University of Miami, 4600

11 Rickenbacker Causeway, Miami, FL 33149, USA

12 ⁴CICERO Center for International Climate and Environmental Research in Oslo, 0318, Oslo,
13 Norway

14 ⁵School of Earth and Environment, University of Leeds, Leeds, LS2 9JT, UK

15 ⁶International Institute for Applied Systems Analysis (IIASA), Laxenburg, 2351, Austria
16

17 Corresponding Author: Ryan J. Kramer (ryan.j.kramer@nasa.gov)

18
19 **Key Points**

- 20 • Observed instantaneous radiative forcing has increased, strengthening the top-of-
21 atmosphere radiative imbalance.
- 22 • Due to cancellations in longwave and shortwave radiation, the sum of rapid adjustments
23 and radiative feedbacks exhibit an insignificant trend.
- 24 • Observed increases in instantaneous radiative forcing are direct evidence of the
25 anthropogenic effects on the Earth's radiative energy budget.

26

27

28

29

30

31

32

33 **Abstract**

34

35 Changes in atmospheric composition, such as increasing greenhouse gases, cause an initial
36 radiative imbalance to the climate system, quantified as the instantaneous radiative forcing. This
37 fundamental metric has not been directly observed globally and previous estimates have come
38 from models. In part, this is because current space-based instruments cannot distinguish the
39 instantaneous radiative forcing from the climate's radiative response. We apply radiative kernels
40 to satellite observations to disentangle these components and find all-sky instantaneous radiative
41 forcing has increased 0.53 ± 0.11 W/m² from 2003 through 2018, accounting for positive trends in
42 the total planetary radiative imbalance. This increase has been due to a combination of rising
43 concentrations of well-mixed greenhouse gases and recent reductions in aerosol emissions. These
44 results highlight distinct fingerprints of anthropogenic activity in Earth's changing energy
45 budget, which we find observations can detect within 4 years.

46

47 **Plain Language Summary**

48 Climate change is a response to energy imbalances in the climate system. For example, rising
49 greenhouse gases directly cause an initial imbalance, the radiative forcing, in the planetary
50 radiation budget, and surface temperatures increase in response as the climate attempts to restore
51 balance. The radiative forcing and subsequent radiative feedbacks dictate the amount of
52 warming. While there are well-established observational records of greenhouse gas
53 concentrations and surface temperatures, there is not yet a global measure of the radiative
54 forcing, in part because current satellite observations of Earth's radiation only measure the sum
55 total of radiation changes that occur. We use the radiative kernel technique to isolate radiative

56 forcing from total radiative changes and find it has increased from 2003 through 2018,
57 accounting for nearly all of the long-term growth in the total top-of-atmosphere radiation
58 imbalance during this period. We confirm that rising greenhouse gas concentrations account for
59 most of the increases in the radiative forcing, along with reductions in reflective aerosols. This
60 serves as direct evidence that anthropogenic activity has affected Earth’s energy budget in the
61 recent past.

62 **1. Introduction**

63 The Instantaneous Radiative forcing (IRF) is the initial imbalance of the Earth’s top-of-
64 the-atmosphere (TOA) radiative energy budget directly caused by a change in atmospheric
65 composition, such as increasing greenhouse gases (GHGs), or perturbed surface properties, like
66 from land use change. All anthropogenic climate changes are a response to the IRF, including
67 surface temperature change and associated radiative feedbacks (Sherwood et al. 2015). Despite a
68 sound basis in physics and radiative transfer theory, the IRF is hard to directly diagnose from
69 observations. Multiple remote sensing and in-situ instruments observe net radiative fluxes, but
70 these measurements convolve the IRF with radiative responses to the changing atmospheric
71 state. Some studies have diagnosed a more broadly defined “greenhouse effect” by evaluating
72 observations of clear-sky longwave radiation at the surface (Philipona et al. 2004) and TOA
73 (Raghuraman et al. 2019), but this analysis does not separate the IRF from water vapor feedback
74 processes.

75 Harries et al. (2001) compared outgoing longwave radiation at the TOA from two
76 satellite instruments launched decades apart, attributing emission differences at relevant spectral
77 bands to rising greenhouse gas (GHG) concentrations. However, instrumental uncertainty
78 between the two platforms complicates interpretation (Jiang et al. 2011). Feldman et al. (2015,
79 80

81 2018) used ground observations from the US Department of Energy Atmospheric Radiation
82 Measurement (ARM) program to provide the most observationally-oriented assessment to date
83 of GHG surface radiative forcing, which is proportional to the TOA IRF. However, their
84 analysis was limited to longwave (LW) forcing from CO₂ and CH₄ and was only conducted for
85 two locations. The total IRF has not been directly diagnosed globally from observations.

86 Well understood radiative transfer theory tightly constraints the GHG component of the IRF.
87 Line-by-line radiative transfer models diagnose it within 1% agreement (Collins et al. 2006;
88 Mlynczak et al. 2016; Pincus et al. 2020). However, these highly accurate calculations are
89 computationally expensive, so analysis is often limited to a few idealized atmospheric profiles.
90 Quantifying the IRF globally and over time relies on more efficient but less accurate
91 parameterized radiative transfer models (Soden et al. 2018), which introduces model bias when
92 applied to observations. Diagnosing the IRF from aerosols with these models suffers from the
93 same pitfalls, plus additional uncertainty associated with aerosol optical properties that are not
94 well-observed (Randles et al. 2013; Stier et al. 2013). While there have been recent efforts to
95 constrain aerosol IRF with observations (Bellouin et al. 2020; Watson-Parris et al. 2020), results
96 are usually not temporally resolved.

97 Here we circumvent these limitations by applying radiative kernels (Soden et al. 2008) to
98 isolate the IRF from radiative feedbacks and rapid adjustments over time. We demonstrate that
99 the IRF has increased with rising GHG concentrations, accounting for recent, positive trends in
100 the total TOA radiative imbalance. More specifically, we consider this IRF to be largely a
101 consequence of concentration changes after anthropogenic emissions are moderated by natural
102 carbon cycle responses (Friedlingstein et al. 2019).

103

2. Methods

Variations in the total, all-sky radiative energy balance at the TOA, dR , constrain global surface temperature change and consists of the all-sky instantaneous radiative forcing (IRF) and radiative responses to the IRF:

$$dR = IRF + dR_\lambda \quad (1),$$

where dR_λ is net radiative changes caused by surface temperature-mediated radiative feedbacks and rapid adjustments from, to first order, temperature (T), water vapor (q), surface albedo (α) and cloud (C) changes (Vial et al. 2013; Sherwood et al. 2015):

$$dR_\lambda = dR_T + dR_q + dR_\alpha + dR_C \quad (2).$$

For simplicity, we will not decompose these terms further into feedbacks and rapid adjustments since it has no bearing on diagnosing the IRF. We simply refer to these radiative anomalies as radiative responses. We note that dR_λ includes both anthropogenic responses and natural variability (e.g. Trenberth et al. 2015).

The Clouds and Earth's Radiant Energy System (CERES) has provided global TOA energy balance observations since 2000. Here, we diagnose dR using radiative flux anomalies from the CERES Energy Balance and Filled (EBAF) Ed. 4.1 product (Loeb et al. 2018a; Loeb et al. 2019). While no observational product measures the radiative response terms in isolation, they can be diagnosed using radiative kernels combined with observations of the relevant state

128 variable, x (B. Zhang et al. 2019; Bony et al. 2020). An individual, non-cloud radiative response,
129 dR_x , in linear form is:

130

$$131 \quad dR_x = \frac{\partial R}{\partial x} dx = K_x dx, \quad x = T, q, \alpha \quad (3),$$

132

133 where K_x is a radiative kernel representing direct radiative changes from small, standard
134 perturbations in state variable x and dx is the actual temperature (T), water vapor (q) or surface
135 albedo (α) climate response. Under clear-sky (CS) conditions:

$$136 \quad dR^{CS} = IRF^{CS} + dR_\lambda^{CS} \quad (4),$$

137

138 where:

$$139 \quad dR_\lambda^{CS} = dR_T^{CS} + dR_q^{CS} + dR_\alpha^{CS} \quad (5).$$

140

141 To diagnose dR_x or dR_x^{CS} we use observational-based radiative kernels developed from
142 the CloudSat Fluxes and Heating Rates product 2B-FLXHR-LIDAR (Kramer et al. 2019).
143 Unlike GCM-derived radiative kernels, these kernels are free from model bias in the base state,
144 and thus ideal for diagnosing observed radiation changes. Calculating K_x requires using a
145 radiative transfer model to convert base state perturbations to radiative sensitivities. Therefore,
146 using radiative kernels introduces some radiative-transfer model dependency. We apply the
147 radiative kernels to deseasonalized anomalies of temperature and specific humidity profiles from
148 version 6 Level 3 AIRS retrievals (Aumann et al. 2003) to estimate dR_T and dR_q and to surface
149 albedo anomalies from CERES EBAF surface fluxes (Kato et al. 2018) to estimate dR_α . Due to
150 computational expense, radiative kernels, including those used here, are often derived from one

151 year of data. However radiative kernel inter-annual variability is small (Pendergrass et al. 2018;
 152 Thorsen et al. 2018), therefore applying radiative kernels to the entire observational record is
 153 justified.

154 In the traditional radiative kernel technique used here, the cloud radiative response (dR_C)
 155 is calculated as the change in cloud radiative effects (CRE) corrected for cloud masking (Soden
 156 et al, 2008; Kramer et al. 2019):

$$158 \quad dR_C = dCRE - (dR_T - dR_T^{CS}) - (dR_q - dR_q^{CS}) - (dR_\alpha - dR_\alpha^{CS}) - (IRF - IRF^{CS}) \quad (6),$$

159
 160 where CRE is the difference between all-sky and clear-sky radiative fluxes. The cloud masking
 161 correction is necessary because CRE includes differences between all-sky and clear-sky non-
 162 cloud radiative changes, which are not actual cloud radiative responses (Soden et al. 2004). Here
 163 $dCRE$ is estimated using the TOA CERES EBAF radiative fluxes. The dR_x terms are diagnosed
 164 using all-sky and clear-sky radiative kernels as described above.

165 The ultimate goal of this study is to derive the IRF from these radiative kernel
 166 calculations. Under clear-sky conditions, we simply diagnose IRF^{CS} by rearranging Equation 3,
 167 whereby:

$$168 \quad IRF^{CS} = dR^{CS} - dR_\lambda^{CS} = dR^{CS} - (dR_T^{CS} + dR_q^{CS} + dR_\alpha^{CS}) \quad (7),$$

169
 170 For all-sky conditions, an analogous calculation would require dR_C to be removed from dR , but
 171 since estimating dR_C as in equation 6 requires the IRF to be known, this differencing technique is
 172 not possible. Following common practice (Soden et al. 2008; Vial et al. 2013), we estimate the
 173 all-sky IRF as:

174
$$IRF = \frac{IRF^{CS}}{Cl} \quad (8),$$

175
176 where Cl is a constant that accounts for cloud masking of the IRF. For the longwave (LW) Cl ,
177 we use a constant of 1.24, derived by dividing clear-sky and all-sky double-call radiative transfer
178 calculations of CO_2 IRF from models (Smith et al. 2018). The cloud mask for the shortwave
179 (SW) is derived from direct output of aerosol IRF from Modern-Era Retrospective Analysis for
180 Research and Applications, Version 2 (MERRA-2) reanalysis (Gelaro et al. 2017). The global-
181 mean value is 2.43, in line with a range of observational-based cloud masking estimates by
182 Bellouin et al. (2020). Only the MERRA-2 SW Cl is available over time, but it has an
183 insignificant long-term trend. Consequently, SW IRF has nearly identical trends when computed
184 with a time resolved versus constant SW Cl .

185 This conversion to all-sky conditions accounts for the presence of clouds but not cloud
186 changes. Therefore, the IRF in this study does not include aerosol-cloud interactions, such as
187 cloud albedo effects (Boucher et al. 2013). Instead, these terms are included in dR_C . Therefore,
188 the aerosol component to the kernel-derived estimates of IRF is akin to aerosol direct radiative
189 effects found throughout the literature (e.g. Thorsen et al. 2020).

190 The AIRS L3 data has the shortest record among satellite observations used in this study,
191 with 2003 being the first complete year of data. Thus, we compute all deseasonalized anomalies
192 from 2003 through 2018 relative to the mean of that time span. While we refer to the resulting
193 calculation as the IRF for brevity, we actually show anomalies of the IRF. For comparison, we
194 also estimate the IRF by applying the CloudSat radiative kernels to MERRA-2 reanalysis over
195 the same period. This reanalysis product assimilates a variety of satellite observations, including
196 observations of aerosol properties.

197 In climate models, idealized simulations and flux diagnostics from double-call radiative
198 transfer calculations can be used to evaluate the accuracy of radiative kernel estimates of dR_{λ} and
199 IRF (e.g. Vial et al. 2013; Smith et al. 2018). Such a comparison is not possible in the observed
200 record or the MERRA-2 reanalysis, however. Since the IRF is derived from differencing the
201 other radiative terms, there will always be near-perfect energy closure, albeit with some error due
202 to cloud masking assumptions, which is typically small (Chung and Soden 2015). Alternatively,
203 we will compare these kernel-derived estimates to various independent measures of the IRF.

204 To verify the aerosol component of the IRF, we compare radiative kernel-derived SW
205 IRF to direct output of the aerosol direct radiative effect from MERRA-2. We also compare SW
206 IRF to trends in aerosol optical depth (AOD) from MERRA-2 and observations from the
207 Moderate Resolution Imaging Spectroradiometer (MODIS) merged Dark Target and Deep Blue
208 product (Sayer et al. 2014).

209 We compare radiative-kernel derived estimates of the LW IRF to offline radiative
210 transfer calculations of GHG IRF. We apply empirical formulas to observed global-mean
211 concentrations of 5 major greenhouse gases (CO_2 , CH_4 , N_2O , CFC-11 and CFC-12), provided by
212 NOAA Global Monitoring Division (Hoffman et al. 2006; Montzka et al. 2011). Etminan et al.
213 (2016) derive the empirical formulas from polynomial fits to line-by-line radiative forcing
214 calculations. While these formulas were originally developed for net stratospherically adjusted
215 radiative forcing, we use corrections from additional line-by-line calculations (Hodnebrog et al.
216 2013; Etminan et al. 2016) to calculate TOA IRF, decomposed into a LW and SW component.

217 We also estimate GHG IRF using the SOCRATES offline radiative transfer model
218 (Edwards et al. 1996; Manners et al. 2015) with NOAA GHG concentrations and atmospheric
219 profiles from the MERRA-2 reanalysis. Like the other IRF estimates, these calculations are

220 presented in anomaly space with the seasonal cycle removed. The IRF from CFCs has decreased
221 recently, but this has been compensated for by a near equal increase from other halocarbons not
222 considered in empirical fit and SOCRATES calculations (Myhre et al. 2013). To account for this,
223 we repeat these calculations with no CFC trend. This only modifies total GHG IRF trends by
224 <5%, however, so hereafter we focus on results without this assumption. The SOCRATES IRF
225 calculations are conducted under pristine, clear-sky conditions and converted to all-sky via
226 Equation 8, like the radiative kernel calculations.

227 The various inputs and assumptions detailed above can contribute uncertainty to the
228 estimated radiative changes. In a Supplemental Appendix we provide a comprehensive
229 uncertainty assessment in the IRF trends due to these contributors, including from observed dR ,
230 radiative kernels, and the cloud masking constant, Cl . We find these uncertainties are smaller
231 than the trend regression uncertainty associated with timeseries variability. Therefore, all trends
232 presented hereafter are provided with 95% confidence intervals (or roughly 2 standard errors
233 around the mean) associated with the least-squares linear regression. This is common practice
234 when diagnosing CERES trends (e.g. Loeb et al. 2018a,b).

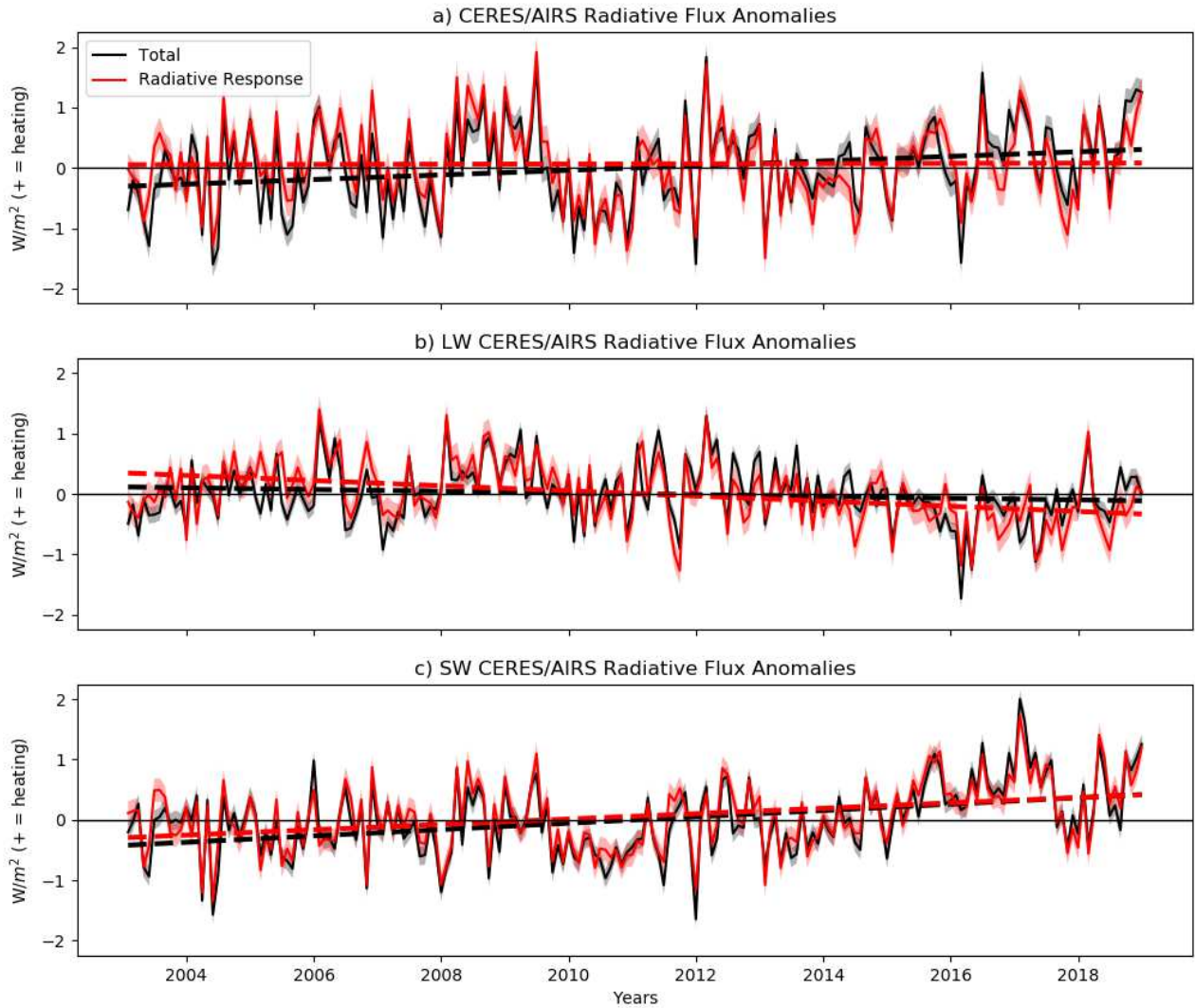
235 The anomalies of dR , dR_λ and the IRF are subject to the same sources of uncertainty as long-
236 term trends. Therefore, Figure 1 and 2 below include uncertainty bounds diagnosed as 2σ across
237 multiple estimates of the radiative terms using different radiative flux data products from CERES
238 and alternative radiative kernel sets and model estimates of Cl (see Supplemental Appendix).

239 **3. Results**

240 Figure 1a shows a timeseries of global-mean total radiative flux anomalies (dR) from CERES
241 satellite observations and its component from radiative responses (dR_λ), estimated by applying
242
243
244

245 the CloudSat-based radiative kernels to CERES and AIRS observations (hereafter
246 CERES/AIRS). Positive anomalies indicate a net increase in downwelling radiation at the TOA
247 (planetary warming). The sum of the radiative responses, dR_λ , accounts for nearly all of the total
248 short-term dR variability, as evident by their strong correlation ($r=0.88$) and small root-mean-
249 squared difference of 0.024 ± 0.003 W/m²; $\sim 3.5\%$ of the standard deviation of dR . On inter-annual
250 timescales, ENSO strongly influences this variability (Trenberth et al. 2014), which lags by ~ 5
251 months (Supplemental Fig. S1; Loeb et al. 2018b). Long-term dR exhibits a positive, linear trend
252 (0.038 ± 0.02 W/m²/year) significant with 95% confidence, while dR_λ exhibits an insignificant
253 trend (0.002 ± 0.02 W/m²/year) an order of magnitude smaller. This arises from cancelation
254 between LW and SW dR_λ . The LW dR_λ has a negative linear trend (-0.042 ± 0.02 W/m²/year)
255 (Fig. 1b), mainly from global warming-driven dR_T decreases (-0.041 ± 0.007 W/m²/year)
256 (Supplemental Fig. S2). The SW dR_λ trend (0.044 ± 0.02 W/m²/year) is nearly equal and opposite
257 of the LW, driven by increases in SW dR_α (0.023 ± 0.09 W/m²/year) and SW dR_C (0.020 ± 0.13
258 W/m²/year), a predominantly low cloud response (Loeb et al. 2018b). The latter alone accounts
259 for most of the SW interannual variability.

260



261

262

263 **Figure 1.** Global-mean a) net, b) longwave (LW) and c) shortwave (SW) total radiative flux
 264 anomalies from 2003 through 2018 as measured by CERES (black) and the contribution to that
 265 total from the sum of radiative responses (red). Respective trendlines are displayed as dashed
 266 lines. Uncertainty of $\pm 2\sigma$ is shown for each timeseries, computed as described in the Methods.
 267 Linear trends and 95% confidence intervals are provided in text.

268

269

270

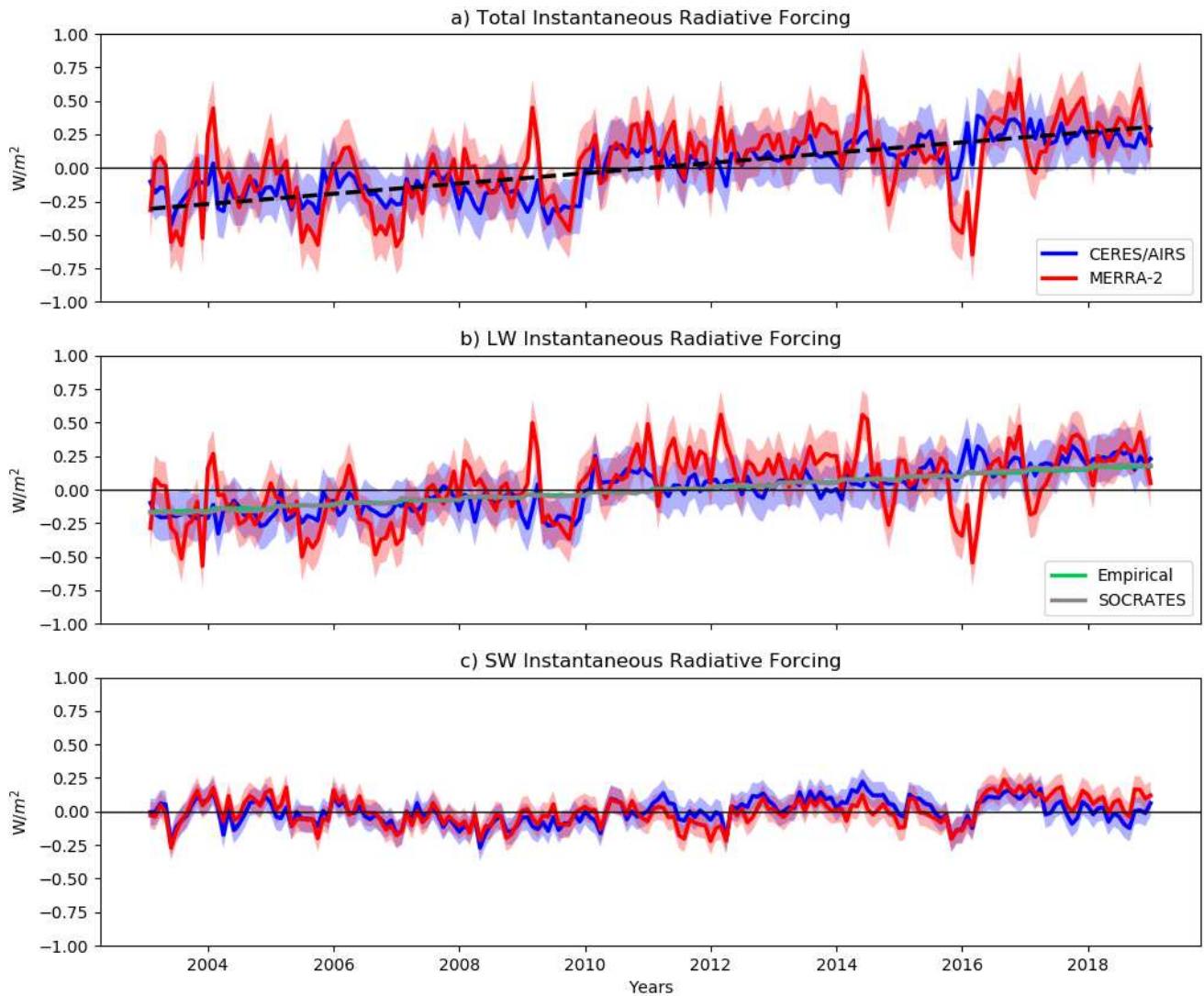
271

272

MERRA-2 also exhibits a significant, positive trend in dR but not dR_λ due to compensating LW and SW components (Supplemental Fig. S3). However, there is a positive trend in LW dR_λ and a negative trend in SW dR_λ , opposite from the CERES/AIRS response. This occurs due to a considerably different LW and SW dR_C (Supplemental Fig. S4) compared to satellite observations.

273 Since neither dR_λ or its uncertainties account for the positive dR trend, it must be
274 explained by the IRF. Figure 2 shows the timeseries of the total, LW and SW IRF under all-sky
275 conditions, estimated from the radiative kernel technique. The total CERES/AIRS IRF exhibits a
276 significant, positive trend (0.033 ± 0.007 W/m²/year), mostly from increasing LW IRF
277 (0.027 ± 0.006 W/m²/year). The SW IRF exhibits a smaller, yet still significant increase
278 (0.006 ± 0.003 W/m²/year). The LW IRF trend is opposite in sign from LW dR , since decreasing
279 LW dR_λ compensates. In the SW, IRF and dR are both increasing, but SW dR_λ is the dominant
280 contributor while the IRF trend is much smaller.

281 Rising GHG concentrations explain the positive LW IRF trend. Accordingly, it increases
282 at a similar rate to the GHG IRF estimates from the empirical fit (0.021 ± 0.0002 W/m²/year or
283 0.022 ± 0.0002 W/m²/year if ignoring CFCs [see Methods]) and the SOCRATES radiative
284 transfer model (0.023 ± 0.0003 W/m²/year) (Fig. 2b), despite these calculations neglecting some
285 GHG forcers found in nature, such as ozone. MERRA-2 exhibits a similar LW IRF trend to
286 CERES/AIRS (0.029 ± 0.003 W/m²/year) while direct output of the LW aerosol IRF from
287 MERRA-2 exhibits no trend. This further indicates GHG increases account for roughly all LW
288 IRF increases.



289

290

291 **Figure 2.** Global-mean a) total, b) longwave (LW) and c) shortwave (SW) instantaneous
 292 radiative forcing (IRF) estimated from the radiative kernel technique for CERES/AIRS (red) and
 293 MERRA-2 (blue). Additional calculations of greenhouse gas-only IRF are also shown using
 294 empirical formulas (green) and the SOCRATES radiative transfer model (gray). For reference,
 295 the trendline for total radiative flux anomalies (Fig 1a) is displayed with the total IRF as a black
 296 dashed line. Uncertainty of $\pm 2\sigma$ is shown with shading for each timeseries, computed as
 297 described in the Methods. Linear trends and 95% confidence intervals are provided in text and
 298 in Table 1.

299

Increasing GHG concentrations also contribute (0.002 ± 0.00 W/m²/year) to the total

300

positive SW IRF trends, according to estimates from the empirical fits. The SW GHG trend is

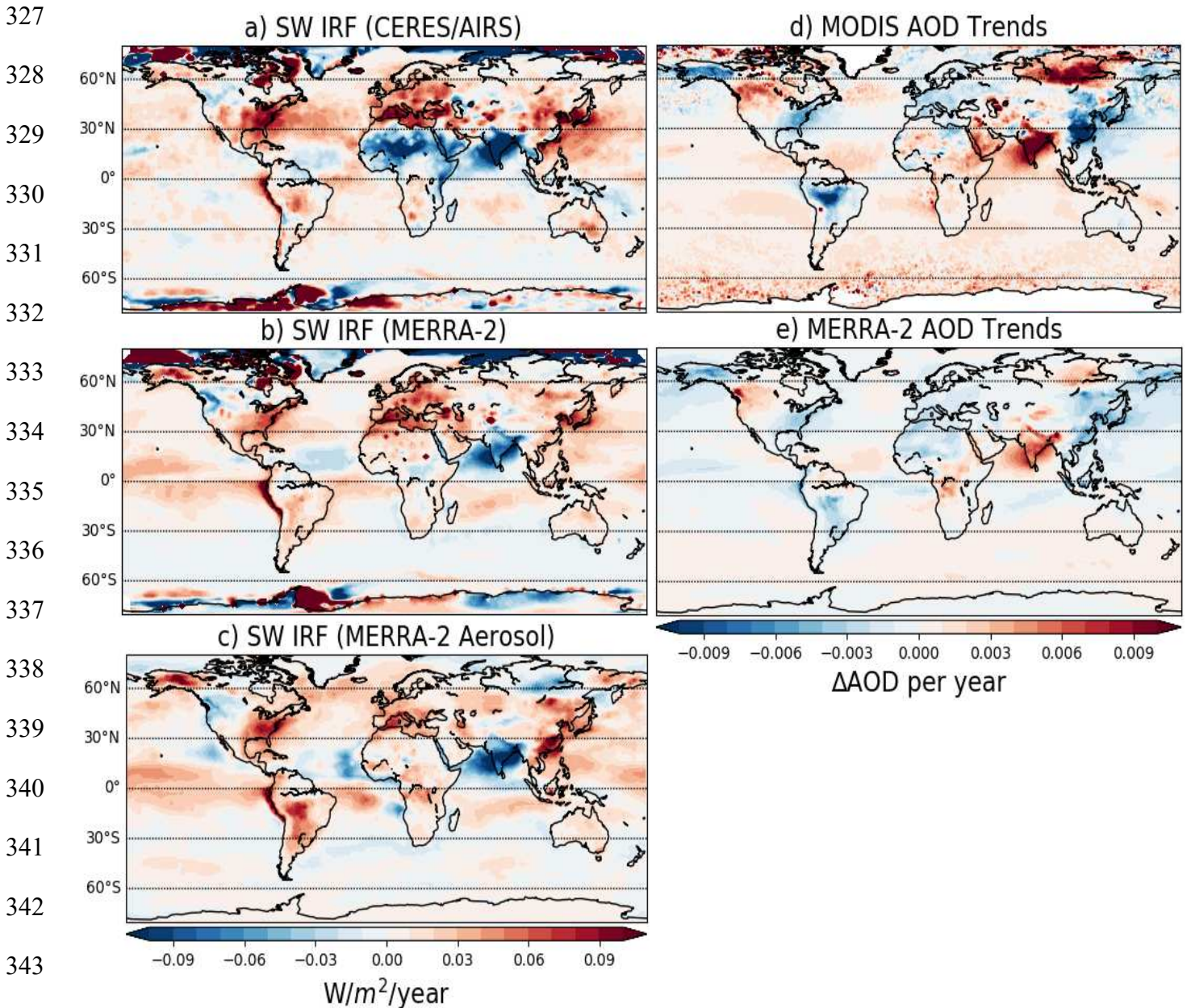
301 negligible in the SOCRATES calculations, but the model version used here does not account for
302 the SW absorption of CH₄.

303 The total SW IRF increase is nearly identical in CERES/AIRS and MERRA-2, and to
304 aerosol-only SW IRF trends from MERRA-2 direct output (Supplemental Fig. S5). They also
305 exhibit similar short-term variability. This suggests aerosols explain most of the SW IRF. The
306 long-term radiative heating is consistent with declining anthropogenic aerosol emissions during
307 this period (Q. Zhang et al. 2019). Towards the end of the timeseries, CERES/AIRS SW IRF has
308 more positive anomalies. Locally, the largest differences with MERRA-2 after 2015 are in major
309 absorbing aerosol source regions (Supplemental Fig. S6), suggesting a contribution from
310 different absorbing aerosol properties.

311 Figure 3 shows local linear trends in kernel-derived, total SW IRF from CERES/AIRS
312 and MERRA-2 and direct MERRA-2 output of aerosol-only SW IRF (Figure 3c). The spatial
313 pattern of the SW IRF trend is generally consistent across all three estimates. A notable
314 hemispheric asymmetry is present, with large changes concentrated in the populous Northern
315 Hemisphere. This includes large positive trends over the Eastern United States, Western Europe
316 and Eastern China, where anthropogenic emissions of reflective aerosols have declined because
317 of government actions to combat poor air quality (Kühn et al. 2014; Ridley et al. 2018; Q. Zhang
318 et al. 2019). In contrast, the SW IRF trends are negative over India, where emissions continue to
319 rise (Dey et al. 2012).

320 There are some magnitude differences in these major source regions, however. For
321 instance, trends are larger in the Eastern US and India in CERES/AIRS than in MERRA-2. This
322 coincides with differences in the MODIS and MERRA-2 AOD trends (Figure 3d,e), which are
323 also larger in CERES/AIRS. Over Saharan Africa, the sign of the SW IRF trend differs,

324 consistent with opposing trends in MODIS and MERRA-2 AOD. Dust radiative forcing during
325 this period is likely a key factor (Supplemental Fig. S7; Shao et al. 2013) and is highly uncertain
326 (Miller et al. 2014; Kok et al. 2017).



345 **Figure 3.** Local linear trends from 2003 through 2018 in all-sky shortwave instantaneous radiative forcing
346 (SW IRF) diagnosed in a) CERES/AIRS observations and b) MERRA-2 reanalysis using the radiative kernel
differencing technique and c) from direct output of MERRA-2 aerosol IRF. Also, local linear trends over the
same time period are shown for aerosol optical depth (AOD) from d) MODIS and e) MERRA-2.

347
348
349 The strong agreement in MERRA-2 trends from kernel differencing versus direct SW
350 aerosol IRF output (Fig 3b,c) highlights the dominant role of aerosols in the total SW IRF trends.
351 It also confirms the accuracy of the radiative kernel technique. The kernel differencing method
352 results in artifacts in the polar regions, however, where large local trends are a consequence of
353 underestimating the SW dR_{α} removed from dR (Supplemental Fig. S8) and not from actual
354 forcing. One possible explanation is surface albedo radiative kernels fail to capture important
355 ice-albedo feedback non-linearities (Block et al. 2013). Nevertheless, the polar region errors
356 have negligible effect on global-mean SW IRF trends.

357 Some inter- and intra-annual variability (hereafter short-term variability) in SW IRF is
358 expected, given natural variations in aerosol concentrations. Consequently, the detrended
359 aerosol-only ($\sigma=0.088$ W/m²) and kernel-derived ($\sigma=0.097$ W/m²) SW IRF in MERRA-2
360 exhibit similar variability and are highly correlated ($r=0.78$). The source of the notable short-
361 term variability in LW IRF (Fig. 2b) is less apparent, however, since greenhouse gas
362 concentrations increase relatively steadily on these timescales, as evident in the empirical fit
363 estimate of GHG IRF, which increases almost perfectly linearly.

364 While radiative kernel error may play some role, the LW IRF from CERES/AIRS
365 exhibits considerably more short-term variability ($\sigma=0.24$) than MERRA-2 ($\sigma=0.16$), despite
366 using the same CloudSat-derived radiative kernels in both estimates. This highlights short-term
367 inconsistencies between the radiative fluxes observed by CERES (dR^{cs}) and the AIRS retrievals
368 used to diagnose LW dR_{λ}^{cs} . For instance, the difference between CERES/AIRS and MERRA-2
369 dR_{λ}^{cs} exhibits considerably more short-term variability than the difference between dR^{cs} . This is
370 mostly due to different variability in dR_{τ}^{cs} (Supplemental Fig. S9), and more specifically due to

371 different temperature anomalies at the surface and in the boundary layer between AIRS and
372 MERRA-2 (Supplemental Fig. S10). Since AIRS temperature anomalies are more variable, so is
373 the dR_T^{cs} estimate. And since this variability is not also observed radiatively by CERES, it is not
374 evident in dR^{cs} . This ultimately translates to a more variable LW IRF when using the kernel
375 differencing technique. This also explains why LW IRF spatial patterns are noisier for
376 CERES/AIRS than for MERRA-2 (Supplemental Fig. S11). Cloud contamination likely
377 contributes to the AIRS temperature variability, as found previously (Hearty et al. 2014). This is
378 evident at the surface, for example, where the largest differences between AIRS and MERRA-2
379 temperature anomalies tend to occur where clouds are common (Supplemental Fig. S9),
380 especially over land. While global-mean surface temperature anomalies from AIRS closely agree
381 with other, independent datasets (Susskind et al. 2019), it is possible the temperature biases that
382 do exist are magnified in the context of radiative changes.

383 The LW IRF variability may also stem from its sensitivity to the atmospheric base state
384 (Pincus et al. 2015). However, this contribution appears to be small. In the LW GHG IRF
385 estimated from the SOCRATES radiative transfer model, we use daily MERRA-2 temperature,
386 surface albedo and humidity data, thus capturing the GHG IRF sensitivity to the unperturbed,
387 non-cloud base state. Still, the short-term variability from this offline calculation is nearly as
388 small as estimates with the empirical fit, which does not account for base state variability. The
389 LW IRF short-term variability in this comparison (and in the radiative kernel-derived estimates)
390 is not due to variations in the cloud base state since LW cloud masking is always treated as a
391 constant. While clouds may play a greater role in reality, the SW IRF estimated from radiative
392 kernels with constant cloud masking has similar short-term variability to the aerosol-only SW
393 IRF in MERRA-2, which accounts for cloud masking temporal variations. This suggests cloud

394 variability may not be important in the global-mean. Lastly, some LW IRF variability in
 395 MERRA-2 (and in CERES/AIRS) may be due to spatial variability in the GHG concentrations
 396 (Myhre et al. 2013), which is not present in the empirical fit or the SOCRATES estimates.

397

	LW	SW	Net
CERES/AIRS	0.027±0.006	0.006±0.003	0.033±0.007
MERRA-2	0.029±0.003	0.006±0.003	0.035±0.004
Aerosol-Only MERRA-2	-4.2E-4±1.5E-4	0.006±0.003	0.006±0.003

398 **Table 1.** Global-mean linear trends ($W/m^2/year$) and 95% confidence bounds in
 399 instantaneous radiative forcing estimated using the radiative kernel differencing
 400 technique (first two rows) and MERRA-2 flux diagnostics (third row).

401

402

403

404 4. Conclusions

405

406 We have diagnosed the global instantaneous radiative forcing (IRF) directly from
 407 observations using radiative kernels. Table 1 summarizes linear trends. We find that from 2003
 408 through 2018, the observed IRF has increased $0.53 \pm 0.11 W/m^2$, almost entirely accounting for
 409 the positive trend in CERES Top-of-Atmosphere (TOA) radiative flux anomalies (dR). The
 410 intrinsic LW and SW climate radiative responses largely cancel out. This IRF increase mostly
 411 occurs in the LW ($0.43 \pm 0.1 W/m^2$), driven by rising greenhouse gas concentrations. This serves
 412 as direct observational evidence that anthropogenic activity is impacting the Earth's energy
 413 balance. The SW IRF has also increased ($0.1 \pm 0.05 W/m^2$). In part, this is a reflection of
 414 government-mandated aerosol emission reductions throughout major source regions, which may
 415 have a greater direct impact than inferred by the SW IRF, which does not include aerosol cloud-
 416 albedo effects in this analysis.

417 Diagnosing the observed IRF is important for our fundamental understanding of Earth's
418 response to climate change and a valuable piece of information for policy decisions.
419 Conceivably, observed IRF could be used as a top-down approach for monitoring the climate
420 response to mitigation efforts. By applying published metrics of instrumental uncertainty in
421 AIRS (Tobin et al. 2006; Hearty et al. 2014) and CERES (Loeb et al. 2018), along with the
422 kernel-derived IRF variance and trend, we apply formulas by Leroy et al. (2008) to determine the
423 minimum length of the observational record necessary to detect a climate change signal. These
424 formulas account for trend uncertainty due to natural variability and instrumental uncertainty.
425 Using this approach, we find total IRF trends are detectable, given these sources of uncertainty,
426 within 3.8 years using the satellite data presented in this study. Therefore, the methods
427 introduced here could be useful for near-real time monitoring, especially since the time to
428 detection shortens with the lengthening of the observational record.

429

430 **Acknowledgements:** We thank the Editor, reviewers and Graeme Stephens for valuable
431 feedback on this work. RJK is supported by an appointment to the NASA Postdoctoral Program
432 administered by Universities Space Research Association. HH and BJS are supported by NASA
433 award 80NSSC18K1032. LO gratefully acknowledges support from NASA's
434 CloudSat/CALIPSO Science Team and MEaSUREs programs. GM, PMF and CJS were
435 supported by European Union's Horizon 2020 Research and Innovation Programme under grant
436 agreement no. 820829 (CONSTRAIN). PMF and CJS were also supported by UKRI NERC
437 grant NE/N006038/1 (SMURPHS). C.J.S. was supported by a NERC/IASA Collaborative
438 Research Fellowship (NE/T009381/1).

439

440 **Competing Interests:** Authors have no competing interests.

441

442 **Data and Materials Availability:** The CERES radiative flux observations are available at
443 <https://ceres.larc.nasa.gov/data/>. The AIRS temperature and water vapor observations and the
444 MERRA-2 reanalysis data are available at <https://disc.gsfc.nasa.gov/>. The CloudSat/CALIPSO
445 radiative kernels used in this study and related code for applying them are available at
446 <https://climate.rsmas.miami.edu/data/radiative-kernels/>.

447

448 **References**

449

450 Aumann, H.H., Chahine, M.T., Gautier, C., M. Goldberg, D., Kalnay, E., McMillin, L.M., et al.
451 (2003). AIRS/AMSU/HSB on the Aqua mission: design, science objectives, data products, and
452 processing systems. *IEEE Transactions on Geoscience and Remote Sensing*, 41(2), 253–264.
453 <https://doi.org/10.1109/TGRS.2002.808356>

454

455 Bellouin, N., Quaas, J., Gryspeerdt, E., Kinne, S., Stier, P., Watson-Parris, D., et al. (2020).
456 Bounding Global Aerosol Radiative Forcing of Climate Change. *Reviews of Geophysics*, 58(1),
457 e2019RG000660. <https://doi.org/10.1029/2019RG000660>

458

459 Block, K., & Mauritsen, T. (2013). Forcing and feedback in the MPI-ESM-LR coupled model
460 under abruptly quadrupled CO₂. *Journal of Advances in Modeling Earth Systems*, 5(4), 676–691.
461 <https://doi.org/10.1002/jame.20041>

462

463 Bony, S., Semie, A., Kramer, R. J., Soden, B., Tompkins, A. M., & Emanuel, K. A. (2020).
464 Observed Modulation of the Tropical Radiation Budget by Deep Convective Organization and
465 Lower-Tropospheric Stability. *AGU Advances*, 1(3). <https://doi.org/10.1029/2019AV000155>

466

467 Boucher, O., Randall, D., Artaxo, P., Bretherton, C., Feingold, G., Forster, P., et al., (2013)
468 Clouds and aerosols. In *Climate Change 2013: The Physical Science Basis. Contribution of*
469 *Working Group I to the Fifth Assessment Report of the Intergovernmental Panel on Climate*
470 *Change*. T.F. Stocker, D. Qin, G.-K. Plattner, M. Tignor, S.K. Allen, J. Doschung, A. Nauels, Y.
471 Xia, V. Bex, and P.M. Midgley, Eds. Cambridge University Press, pp. 571-657,
472 doi:10.1017/CBO9781107415324.016.

473

474 Chung, E.-S., & Soden, B. J. (2015). An Assessment of Direct Radiative Forcing, Radiative
475 Adjustments, and Radiative Feedbacks in Coupled Ocean–Atmosphere Models*. *Journal of*
476 *Climate*, 28(10), 4152–4170. <https://doi.org/10.1175/JCLI-D-14-00436.1>

477

478 Collins, W. D., Ramaswamy, V., Schwarzkopf, M. D., Sun, Y., Portmann, R. W., Fu, Q., et al.
479 (2006). Radiative forcing by well-mixed greenhouse gases: Estimates from climate models in the
480 Intergovernmental Panel on Climate Change (IPCC) Fourth Assessment Report (AR4). *Journal*
481 *of Geophysical Research*, 111(D14), D14317. <https://doi.org/10.1029/2005JD006713>
482

483 Dey, S., Di Girolamo, L., van Donkelaar, A., Tripathi, S. N., Gupta, T., & Mohan, M. (2012).
484 Variability of outdoor fine particulate (PM_{2.5}) concentration in the Indian Subcontinent: A
485 remote sensing approach. *Remote Sensing of Environment*, 127, 153–161.
486 <https://doi.org/10.1016/j.rse.2012.08.021>
487

488 Edwards, J. M., & Slingo, A. (1996). Studies with a flexible new radiation code. I: Choosing a
489 configuration for a large-scale model. *Quarterly Journal of the Royal Meteorological Society*,
490 122(531), 689–719. <https://doi.org/10.1002/qj.49712253107>
491

492 Etminan, M., Myhre, G., Highwood, E. J., & Shine, K. P. (2016). Radiative forcing of carbon
493 dioxide, methane, and nitrous oxide: A significant revision of the methane radiative forcing.
494 *Geophysical Research Letters*, 43(24), 12,614–12,623. <https://doi.org/10.1002/2016GL071930>
495

496 Feldman, D. R., Collins, W. D., Gero, P. J., Torn, M. S., Mlawer, E. J., & Shippert, T. R. (2015).
497 Observational determination of surface radiative forcing by CO₂ from 2000 to 2010. *Nature*,
498 519(7543), 339–343. <https://doi.org/10.1038/nature14240>
499

500 Gelaro, R., McCarty, W., Suárez, M. J., Todling, R., Molod, A., Takacs, L., et al. (2017). The
501 Modern-Era Retrospective Analysis for Research and Applications, Version 2 (MERRA-2).
502 *Journal of Climate*, 30(14), 5419–5454. <https://doi.org/10.1175/JCLI-D-16-0758.1>
503

504 Harries, J. E., Brindley, H. E., Sahoo, P. J., & Bantges, R. J. (2001). Increases in greenhouse
505 forcing inferred from the outgoing longwave radiation spectra of the Earth in 1970 and 1997.
506 *Nature*, 410(6826), 355–357. <https://doi.org/10.1038/35066553>
507

508 Hearty, T. J., Savtchenko, A., Tian, B., Fetzer, E., Yung, Y. L., Theobald, M., et al. (2014).
509 Estimating sampling biases and measurement uncertainties of AIRS/AMSU-A temperature and
510 water vapor observations using MERRA reanalysis. *Journal of Geophysical Research:*
511 *Atmospheres*, 119(6), 2725–2741. <https://doi.org/10.1002/2013JD021205>
512

513 Hodnebrog, Ø., Etminan, M., Fuglestad, J. S., Marston, G., Myhre, G., Nielsen, C. J., et al.
514 (2013). Global warming potentials and radiative efficiencies of halocarbons and related
515 compounds: A comprehensive review. *Reviews of Geophysics*, 51(2), 300–378.
516 <https://doi.org/10.1002/rog.20013>
517

518 Hofmann, D. J., Butler, J. H., Dlugokencky, E. J., Elkins, J. W., Masarie, K., Montzka, S. A., &
519 Tans, P. (2006). The role of carbon dioxide in climate forcing from 1979 to 2004: introduction of
520 the Annual Greenhouse Gas Index. *Tellus B: Chemical and Physical Meteorology*, 58(5), 614–
521 619. <https://doi.org/10.1111/j.1600-0889.2006.00201.x>
522
523

524 Jiang, Y., Aumann, H.H., Wingyee-Lau, M., & Yung, Y.L. (2011). Climate change sensitivity
525 evaluation from AIRS and IRIS measurements. *Proc. SPIE* 8153, XVI (2011), doi:
526 <http://dx.doi.org/10.1117/12.892817>
527

528 Kato, S., Rose, F. G., Rutan, D. A., Thorsen, T. J., Loeb, N. G., Doelling, D. R., et al. (2018).
529 Surface Irradiances of Edition 4.0 Clouds and the Earth's Radiant Energy System (CERES)
530 Energy Balanced and Filled (EBAF) Data Product. *Journal of Climate*, 31(11), 4501–4527.
531 <https://doi.org/10.1175/JCLI-D-17-0523.1>
532

533 Kok, J. F., Ridley, D. A., Zhou, Q., Miller, R. L., Zhao, C., Heald, C. L., et al. (2017). Smaller
534 desert dust cooling effect estimated from analysis of dust size and abundance. *Nature*
535 *Geoscience*, 10(4), 274–278. <https://doi.org/10.1038/ngeo2912>
536

537 Kramer, R. J., Matus, A. V., Soden, B. J., & L'Ecuyer, T. S. (2019). Observation-Based
538 Radiative Kernels From CloudSat/CALIPSO. *Journal of Geophysical Research: Atmospheres*,
539 2018JD029021. <https://doi.org/10.1029/2018JD029021>
540

541 Kühn, T., Partanen, A.-I., Laakso, A., Lu, Z., Bergman, T., Mikkonen, S., et al. (2014). Climate
542 impacts of changing aerosol emissions since 1996. *Geophysical Research Letters*, 41(13), 4711–
543 4718. <https://doi.org/10.1002/2014GL060349>
544

545 Leroy, S.S., Anderson, J.G., & Ohring, G. (2008) Climate Signal Detection Times and
546 Constraints on Climate Benchmark Accuracy Requirements. *Journal of Climate*. 21, 841–846
547

548 Loeb, N. G., Doelling, D. R., Wang, H., Su, W., Nguyen, C., Corbett, J. G., et al. (2018a).
549 Clouds and the Earth's Radiant Energy System (CERES) Energy Balanced and Filled (EBAF)
550 Top-of-Atmosphere (TOA) Edition-4.0 Data Product. *Journal of Climate*, 31(2), 895–918.
551 <https://doi.org/10.1175/JCLI-D-17-0208.1>
552

553 Loeb, N., Thorsen, T., Norris, J., Wang, H., & Su, W. (2018b) Changes in Earth's Energy
554 Budget during and after the “Pause” in Global Warming: An Observational
555 Perspective, *Climate* 6, 62.
556

557 Loeb, N. G., Rose, F. G., Kato, S., Rutan, D. A., Su, W., Wang, H., et al. (2019). Toward a
558 Consistent Definition between Satellite and Model Clear-Sky Radiative Fluxes. *Journal of*
559 *Climate*, 33(1), 61–75. <https://doi.org/10.1175/JCLI-D-19-0381.1>
560

561 Manners J, Edwards JM, Hill P, Thelen J-C. (2015). SOCRATES (Suite Of Community
562 RAdiative Transfer codes based on Edwards and Slingo) Technical Guide. Met Office, UK.
563

564 Miller, R. L., Knippertz, P., Pérez García-Pando, C., Perlwitz, J. P., & Tegen, I. (2014). Impact
565 of Dust Radiative Forcing upon Climate. In P. Knippertz & J.-B. W. Stuut (Eds.), *Mineral Dust:*
566 *A Key Player in the Earth System* (pp. 327–357). Dordrecht: Springer Netherlands.
567 https://doi.org/10.1007/978-94-017-8978-3_13
568

569 Montzka, S. A., Dlugokencky, E. J., & Butler, J. H. (2011). Non-CO₂ greenhouse gases and
570 climate change. *Nature*, 476(7358), 43–50. <https://doi.org/10.1038/nature10322>
571

572 Myhre, G., Shindell, D., Bréon, F.-M., Collins, W., Fuglestedt, J., Huang, J., Koch, D.,
573 Lamarque, J.-F., Lee, E., et al., 2013: Anthropogenic and natural radiative forcing. In *Climate*
574 *Change 2013: The Physical Science Basis. Contribution of Working Group I to the Fifth*
575 *Assessment Report of the Intergovernmental Panel on Climate Change*. T.F. Stocker, D. Qin, G.-
576 K. Plattner, M. Tignor, S.K. Allen, J. Doschung, A. Nauels, Y. Xia, V. Bex, and P.M. Midgley,
577 Eds. Cambridge University Press, pp. 659-740, doi:10.1017/CBO9781107415324.018
578

579 Myhre, G., Kramer, R. J., Smith, C. J., Hodnebrog, Ø., Forster, P., Soden, B. J., et al. (2018).
580 Quantifying the Importance of Rapid Adjustments for Global Precipitation Changes.
581 *Geophysical Research Letters*, 45(20). <https://doi.org/10.1029/2018GL079474>
582

583 Philipona, R., Dürr, B., Marty, C., Ohmura, A., & Wild, M. (2004). Radiative forcing - measured
584 at Earth's surface - corroborate the increasing greenhouse effect. *Geophysical Research Letters*,
585 31(3). <https://doi.org/10.1029/2003GL018765>
586

587 Pincus, R., Mlawer, E. J., Oreopoulos, L., Ackerman, A. S., Baek, S., Brath, M., et al. (2015).
588 Radiative flux and forcing parameterization error in aerosol-free clear skies. *Geophysical*
589 *Research Letters*, 42(13), 5485–5492. <https://doi.org/10.1002/2015GL064291>
590

591 Pincus, R., Buehler, S. A., Brath, M., Jamil, O., Evans, F., Manners, J., et al. (2020). Benchmark
592 calculations of radiative forcing by greenhouse gases. *Earth and Space Science Open Archive*,
593 15. <https://doi.org/10.1002/essoar.10501550.1>
594

595 Randles, C. A., Kinne, S., Myhre, G., Schulz, M., Stier, P., Fischer, J., et al. (2013).
596 Intercomparison of shortwave radiative transfer schemes in global aerosol modeling: results from
597 the AeroCom Radiative Transfer Experiment. *Atmospheric Chemistry and Physics*, 13(5), 2347–
598 2379. <https://doi.org/10.5194/acp-13-2347-2013>
599

600 Raghuraman, S. P., Paynter, D., & Ramaswamy, V. (2019). Quantifying the Drivers of the Clear
601 Sky Greenhouse Effect, 2000–2016. *Journal of Geophysical Research: Atmospheres*, 124(21),
602 11354–11371. <https://doi.org/10.1029/2019JD031017>
603

604 Ridley, D. A., Heald, C. L., Ridley, K. J., & Kroll, J. H. (2018). Causes and consequences of
605 decreasing atmospheric organic aerosol in the United States. *Proceedings of the National*
606 *Academy of Sciences*, 115(2), 290. <https://doi.org/10.1073/pnas.1700387115>
607

608 Shao, Y., Klose, M., & Wyrwoll, K.-H. (2013). Recent global dust trend and connections to
609 climate forcing. *Journal of Geophysical Research: Atmospheres*, 118(19), 11,107-11,118.
610 <https://doi.org/10.1002/jgrd.50836>
611

612 Sherwood, S. C., Bony, S., Boucher, O., Bretherton, C., Forster, P. M., Gregory, J. M., &
613 Stevens, B. (2015). Adjustments in the Forcing-Feedback Framework for Understanding Climate

614 Change. *Bulletin of the American Meteorological Society*, 96(2), 217–228.
615 <https://doi.org/10.1175/BAMS-D-13-00167.1>
616
617 Smith, C. J., Kramer, R. J., Myhre, G., Forster, P. M., Soden, B. J., Andrews, T., et al. (2018).
618 Understanding Rapid Adjustments to Diverse Forcing Agents. *Geophysical Research Letters*,
619 45(21), 12,023–12,031. <https://doi.org/10.1029/2018GL079826>
620
621 Soden, B. J., Broccoli, A. J., & Hemler, R. S. (2004). On the Use of Cloud Forcing to Estimate
622 Cloud Feedback. *Journal of Climate*, 17(19), 3661–3665. [https://doi.org/10.1175/1520-0442\(2004\)017<3661:OTUOCF>2.0.CO;2](https://doi.org/10.1175/1520-0442(2004)017<3661:OTUOCF>2.0.CO;2)
623
624
625 Soden, B. J., Held, I. M., Colman, R., Shell, K. M., Kiehl, J. T., & Shields, C. A. (2008).
626 Quantifying Climate Feedbacks Using Radiative Kernels. *Journal of Climate*, 21(14), 3504–
627 3520. <https://doi.org/10.1175/2007JCLI2110.1>
628
629 Soden, B. J., Collins, W. D., & Feldman, D. R. (2018). Reducing uncertainties in climate models.
630 *Science*, 361(6400), 326–327. <https://doi.org/10.1126/science.aau1864>
631
632 Stier, P., Schutgens, N. A. J., Bellouin, N., Bian, H., Boucher, O., Chin, M., et al. (2013). Host
633 model uncertainties in aerosol radiative forcing estimates: results from the AeroCom Prescribed
634 intercomparison study. *Atmospheric Chemistry and Physics*, 13(6), 3245–3270.
635 <https://doi.org/10.5194/acp-13-3245-2013>
636
637 Susskind, J., Schmidt, G. A., Lee, J. N., & Iredell, L. (2019). Recent global warming as
638 confirmed by AIRS. *Environmental Research Letters*, 14(4), 044030.
639 <https://doi.org/10.1088/1748-9326/aafd4e>
640
641 Tobin, D. C., Revercomb, H. E., Knuteson, R. O., Lesht, B. M., Strow, L. L., Hannon, S. E., et
642 al. (2006). Atmospheric Radiation Measurement site atmospheric state best estimates for
643 Atmospheric Infrared Sounder temperature and water vapor retrieval validation. *Journal of*
644 *Geophysical Research: Atmospheres*, 111(D9). <https://doi.org/10.1029/2005JD006103>
645
646 Thorsen, T. J., Winker, D. M., & Ferrare, R. A. (2020). Uncertainty in observational estimates of
647 the aerosol direct radiative effect and forcing. *Journal of Climate*, 1–63.
648 <https://doi.org/10.1175/JCLI-D-19-1009.1>
649
650 Trenberth, K. E., Fasullo, J. T., & Balmaseda, M. A. (2014). Earth's Energy Imbalance. *Journal*
651 *of Climate*, 27(9), 3129–3144. <https://doi.org/10.1175/JCLI-D-13-00294.1>
652
653 Vial, J., Dufresne, J.-L., & Bony, S. (2013). On the interpretation of inter-model spread in
654 CMIP5 climate sensitivity estimates. *Climate Dynamics*, 41(11), 3339–3362.
655 <https://doi.org/10.1007/s00382-013-1725-9>
656
657

658 Watson-Parris, D., Bellouin, N., Deaconu, L. T., Schutgens, N. A. J., Yoshioka, M., Regayre, L.
659 A., et al. (2020). Constraining Uncertainty in Aerosol Direct Forcing. *Geophysical Research*
660 *Letters*, 47(9), e2020GL087141. <https://doi.org/10.1029/2020GL087141>

661
662 Zhang, B., Kramer, R. J., & Soden, B. J. (2019). Radiative Feedbacks Associated with the
663 Madden–Julian Oscillation. *Journal of Climate*, 32(20), 7055–7065.
664 <https://doi.org/10.1175/JCLI-D-19-0144.1>

665
666 Zhang, Q., Zheng, Y., Tong, D., Shao, M., Wang, S., Zhang, Y., et al. (2019). Drivers of
667 improved PM_{2.5} air quality in China from 2013 to 2017. *Proceedings of the National Academy*
668 *of Sciences*, 116(49), 24463–24469. <https://doi.org/10.1073/pnas.1907956116>

669
670
671
672 **Figure 2.** Global-mean a) net, b) longwave (LW) and c) shortwave (SW) total radiative flux
673 anomalies from 2003 through 2018 as measured by CERES (black) and the contribution to that
674 total from the sum of radiative responses (red). Respective trendlines are displayed as dashed
675 lines. Uncertainty of $\pm 2\sigma$ is shown for each timeseries, computed as described in the Methods.
676 Linear trends and 95% confidence intervals are provided in text.

677
678 **Figure 2.** Global-mean a) total, b) longwave (LW) and c) shortwave (SW) instantaneous
679 radiative forcing (IRF) estimated from the radiative kernel technique for CERES/AIRS (red) and
680 MERRA-2 (blue). Additional calculations of greenhouse gas-only IRF are also shown using
681 empirical formulas (green) and the SOCRATES radiative transfer model (gray). For reference,
682 the trendline for total radiative flux anomalies (Fig 1a) is displayed with the total IRF as a black
683 dashed line. Uncertainty of $\pm 2\sigma$ is shown with shading for each timeseries, computed as
684 described in the Methods. Linear trends and 95% confidence intervals are provided in text and
685 in Table 1.

686

687 **Figure 3.** Local linear trends from 2003 through 2018 in all-sky shortwave instantaneous
688 radiative forcing (SW IRF) diagnosed in a) CERES/AIRS observations and b) MERRA-2
689 reanalysis using the radiative kernel differencing technique and c) from direct output of
690 MERRA-2 aerosol IRF. Also, local linear trends over the same time period are shown for aerosol
691 optical depth (AOD) from d) MODIS and e) MERRA-2.

692

693 **Table 1.** Global-mean linear trends ($W/m^2/year$) and 95% confidence bounds in instantaneous
694 radiative forcing estimated using the radiative kernel differencing technique (first two rows) and
695 MERRA-2 flux diagnostics (third row).

696

697

698

699

700

701

702

703

704

705

706

707

708

709

710

711

712

713

714

715

716

717

718

719

720

721

722

723
724
725
726
727
728
729
730
731
732
733
734
735
736
737
738
739

740
741
742
743
744
745
746
747
748
749
750
751
752

Supplementary Materials for

Observational evidence of increasing global radiative forcing

Ryan J. Kramer^{1,2,*}, Haozhe He³, Brian J. Soden³, Lazaros Oreopoulos¹, Gunnar Myhre⁴,
Piers M. Forster⁵, Christopher J. Smith^{5,6}

¹Earth Sciences Division, NASA Goddard Space Flight Center, Greenbelt, MD 20771, USA

²Universities Space Research Association, 7178 Columbia Gateway Drive, Columbia, MD 21046, USA

³Rosenstiel School of Marine and Atmospheric Science, University of Miami, 4600 Rickenbacker Causeway, Miami, FL 33149, USA

⁴CICERO Center for International Climate and Environmental Research in Oslo, 0318, Oslo, Norway

⁵School of Earth and Environment, University of Leeds, Leeds, LS2 9JT, UK

⁶International Institute for Applied Systems Analysis (IIASA), Laxenburg, 2351, Austria

Corresponding Author: Ryan J. Kramer (ryan.j.kramer@nasa.gov)

Supplemental Appendix:

SA1. Uncertainty Quantification

Following common practice among previous CERES-focused literature (e.g. Loeb et al. 2018a,b), the trend uncertainty quoted throughout the main text is a measure of the linear regression uncertainty, which is largely driven by the internal variability of the timeseries being analyzed. The 95% confidence intervals are given. It is worthwhile to also evaluate uncertainty due to the various assumptions and diagnostic tools that contribute to the estimate of the IRF. As illustrated by equations 7 and 8 in the main text, all-sky IRF is estimated by subtracting radiative-kernel derived, clear-sky radiative responses from the overall clear-sky TOA radiative imbalance (dR^{CS}). This difference, an estimate of the clear-sky IRF (IRF^{CS}) is then divided by a cloud masking constant, Cl , to convert IRF^{CS} into an all-sky IRF. In this supplementary section,

753 we diagnose uncertainty in IRF trends associated with observations of dR^{CS} , radiative kernels,
754 and Cl. We do so by repeating calculations of the IRF, each time substituting in different values
755 for these terms from different sources as explained below, while keeping all other terms
756 unchanged from the method and data described in the main text. Since the standard trend
757 uncertainty is dependent on these additional sources of uncertainty, it is not practical to combine
758 them to quantify a total, comprehensive measure of uncertainty. We therefore discuss these
759 sources individually, compare their relative magnitude, and summarize the uncertainty budget in
760 Table SA4. We focus on the observational estimate of the IRF.

761 *SA1.1 Uncertainty in dR^{CS}*

762 In this work, observed, total TOA radiative anomalies are diagnosed using radiative flux
763 data from CERES EBAF 4.1. This is identical to CERES EBAF4.0 (Loeb et al. 2018a), except it
764 includes an additional clear-sky radiative flux dataset. While the traditional clear-sky products
765 are comprised only of pixels designated as cloud-free, the new product uses an adjustment factor
766 to mimic a total absence of clouds for all regions, similar to how clear-sky is defined in model
767 simulations (Loeb et al. 2019). While CERES has well documented uncertainty in the magnitude
768 of the TOA radiative flux measurements, our work to estimate the IRF is conducted in anomaly
769 space, where uncertainty in absolute fluxes is irrelevant. Instead, it is the uncertainty due to the
770 stability (or lack thereof) of the observing platform that is important. The presence of spurious
771 trends is frequently assessed by comparing EBAF products to the CERES SSF1deg product,
772 which is considered to be extremely stable (e.g. Loeb et al. 2018a,b). To determine associated
773 uncertainty from stability in the observed timeseries of dR^{CS} , we recompute the IRF using four
774 sources of clear-sky radiative fluxes: CERES EBAF 4.1 assuming clear-skies over the total
775 region, CERES EBAF 4.1 assuming clear-skies over cloud-free regions only (the traditional

776 method), CERES SSF1deg from Terra and CERES SSF1deg from Aqua. All other components
 777 of the IRF calculation are consistent across the four estimates. Linear trends of the global-mean
 778 IRF are summarized in Table SA1.

CERES clear-sky Source	Net	LW	SW
EBAF 4.1 – clear-sky (for total region)	0.033	0.027	0.0061
EBAF 4.1 – clear-sky (for cloud-free areas of region)	0.026	0.019	0.0064
SSF1deg Terra	0.027	0.026	0.0015
SSF1deg Aqua	0.024	0.025	-0.0004
Standard Deviation	0.0041	0.0035	0.0034

779 **Table SA1.** Linear trends from 2003 through 2018 in global mean net, longwave (LW) and
 780 shortwave (SW) all-sky Instantaneous radiative forcing, estimated with differences observational
 781 sources of clear-sky radiative fluxes used to diagnose clear-sky TOA radiative flux anomalies.
 782 Units are $W/m^2/yr$.

783
 784 Across the four estimates, we find a standard deviation of $\sigma = 0.0041 W/m^2/yr$ for the Net
 785 IRF, $\sigma = 0.0035 W/m^2/yr$ in the LW and $\sigma = 0.0034 W/m^2/yr$ in the SW. We consider this to be
 786 an upper bound on uncertainty associated with the stability of the CERES observations, since
 787 stability is not the only source of differences between these datasets. Ultimately, we use the new
 788 EBAF 4.1 clear-sky fluxes, representing cloud absence over all regions, in the main analysis
 789 since it is more consistent with the way clear-sky is defined in radiative kernels, the additional
 790 offline radiative transfer calculations of LW GHG IRF, MERRA-2, and in climate models.

791 *SA1.2 Radiative kernel uncertainty*

792 Radiative kernels based on CloudSat/CALIPSO observations are used in this study to
 793 quantify radiative responses to changes in temperature, water vapor and surface albedo.
 794 Radiative kernels are constant in time (beyond a seasonal cycle) and therefore do not contribute
 795 to any spurious trends in the diagnosis of the IRF. However, there is uncertainty in the magnitude
 796 of the radiative kernels which can contribute to uncertainty in the anomalies and trend of the

797 IRF. To quantify this, we estimate the IRF using four different sets of radiative kernels: those
 798 based on CloudSat/CALIPSO discussed in the main text, as well as radiative kernels derived
 799 from the GFDL (Soden et al. 2008), ECHAM6 (Block and Mauritsen 2013) and HadGEM3
 800 (Smith et al. 2020) climate models. All other components of the calculation are consistent across
 801 the four estimates. Linear trends of global-mean IRF are summarized in Table SA2.
 802

Radiative Kernel	Net	LW	SW
CloudSat/CALIPSO	0.0333	0.0272	0.0061
GFDL	0.0313	0.0286	0.0027
ECHAM6	0.0320	0.0297	0.0023
HadGEM3	0.0323	0.0263	0.0060
Standard Deviation	0.0008	0.0015	0.0020

803 **Table SA2.** *Linear trends from 2003 through 2018 in global mean net, longwave (LW) and*
 804 *shortwave (SW) all-sky Instantaneous radiative forcing, estimated using different sets of*
 805 *radiative kernels. Units are $W/m^2/yr$.*

806 We find a standard deviation in trend across the four estimates of $\sigma = 0.0008 W/m^2/yr$ for
 807 Net IRF, $\sigma = 0.0015 W/m^2/yr$ in the LW and $\sigma = 0.0020 W/m^2/yr$ in the SW.

808 *SA1.3 Uncertainty in the cloud masking term.*

809 The cloud masking constant, Cl , used to estimate all-sky IRF accounts for the effect of
 810 the presence of clouds on the magnitude of the IRF, relative to clear-sky conditions. This
 811 quantity is not directly observable and typically requires separate radiative transfer calculations
 812 to diagnose. Therefore, like radiative kernels, it contains uncertainty due to radiative transfer
 813 error and due to biases in the cloud climatology used in those calculations.

814 A lack of data prohibits accurately computing the cloud masking directly from
815 observations. All- and clear-sky double-call calculations of the IRF from model simulations offer
816 the best alternative. However, as discussed by Soden et al. (2018), these diagnostics are rarely
817 conducted with model simulations. To the best of our knowledge, none are available for realistic,
818 historical forcing scenarios.

819 With these limitations, we assume the LW cloud masking is equivalent to the masking of
820 IRF from CO₂ perturbations in this study, which is the dominant GHG driver over the observed
821 period being evaluated. The Coupled Model Intercomparison Project phase 5 (CMIP5, Taylor et
822 al. 2013) includes the necessary double-call calculations from four models to diagnose CO₂
823 cloud masking, using prescribed sea surface temperature, atmosphere-only simulations where
824 CO₂ concentrations are quadrupled. To diagnose uncertainty in the IRF trends due to Cl, we
825 recompute observed all-sky LW IRF by applying Cl estimated from these four models to the
826 observed clear-sky IRF.

827 For the SW, there are analogous simulations in CMIP5 (and CMIP6) for aerosol forcing
828 scenarios, but there are no double-call calculations available to diagnose Cl. Instead, we use
829 clear-sky and all-sky Direct Radiative Forcing (DRF) in 15 models included in the AeroCOM
830 Phase II project (Myhre et al. 2013). Although DRF only includes anthropogenic aerosols, the
831 model-mean Cl from these simulations is 2.70, close to the value from MERRA-2 for SW IRF
832 used in the main text (2.43).

833 To determine associated uncertainty in IRF trends, we recompute IRF with each LW and
834 SW value of Cl from the model simulations discussed above. Results are summarized in Table
835 SA3.

836

837

838

Model	LW IRF		Model	SW IRF
CanAM4	0.0281		BCC	0.00354
HadGEM2-A	0.0272		CAM4-Oslo	0.00631
INMCM4	0.0253		GEOS_CHEM	0.00627
IPSL-CM5A-LR	0.0243		GISS_MATRIX	0.01081
			GISS-ModelE	0.01024
			GMI	0.00841
			GOCART	0.00913
			HadGEM2	0.00634
			IMPACT-Umich	0.00306
			INCA	0.00726
			ECHAM5-HAM	0.00502
			NCAR-CAM3.5	0.00557
			OsloCTM2	0.00362
			SPRINTARS	0.00290
			TM5	0.00923
Standard Deviation	0.00150		Standard Deviation	0.00253

839 **Table SA3.** Linear trends from 2003 through 2018 in global mean net, longwave (LW) and
840 shortwave (SW) all-sky Instantaneous radiative forcing, estimated using different cloud masking
841 constants derived from 4 CMIP5 models for the LW and 14 AeroCOM models for the SW that
842 provided the radiative flux diagnostics necessary for this calculation.

843 The standard deviation across the 4 estimates of LW IRF is $\sigma = 0.00150 \text{ W/m}^2/\text{yr}$ and $\sigma =$
844 $0.00253 \text{ W/m}^2/\text{yr}$ across the 14 estimates of SW IRF. Since different models are used for the
845 LW and SW component, we estimate the standard deviation of the net IRF ($\sigma = 0.00294$
846 $\text{W/m}^2/\text{yr}$), by summing every possible pair of LW and SW IRF trends listed in Table SA3.

847
848
849
850
851
852
853
854
855
856
857
858
859
860
861
862
863
864
865
866
867
868
869
870

SA1.4 Summary

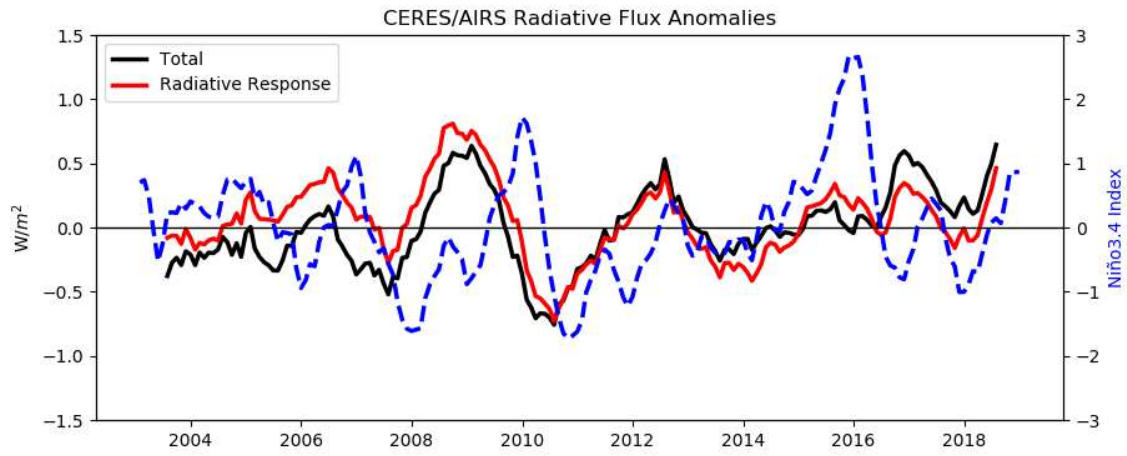
Table SA4 summarizes the results above and additionally shows the trends and 95% confidence intervals for global-mean IRF as outlined in the main text. The 95% confidence intervals represent roughly ± 2 standard errors around the mean. To make the additional measures of uncertainty comparable, the values shown in Table SA4 are doubled from the standard deviations outlined in Tables SA1-3 and are divided by the square root of the number of samples that contributed to each uncertainty calculation (to represent of ± 2 standard errors around the mean)

IRF	Trend	95% Confidence Interval (\pm)	dR ^{CS} uncertainty	Radiative kernel uncertainty	Cloud Mask Uncertainty
Net	0.033	0.007	0.004	0.001	0.0015
LW	0.027	0.006	0.0035	0.0015	0.0015
SW	0.006	0.003	0.0035	0.002	0.0018

Table SA4. *Linear trends and 95% confidence intervals (\pm value) for observed, global-mean net, longwave (LW) and shortwave (SW) Instantaneous Radiative Forcing diagnosed using the methods and data described in the main text as well as uncertainty (± 2 standard errors) from clear-sky TOA radiative anomalies (dR^{CS}), radiative kernels and the cloud masking constant.*

All uncertainties are an order of magnitude smaller than the Net and LW IRF trend and of similar magnitude to the trend in the SW. The IRF trends never cross the zero W/m²/yr threshold given the sources of uncertainty presented. Therefore, the trends are significantly positive. The largest source of uncertainty is in the linear regression itself, represented by the 95% confidence intervals, followed by uncertainty in dR^{CS}. For the Net IRF, this is arguably to be expected, since the trend from the radiative kernel-derived radiative responses is insignificant.

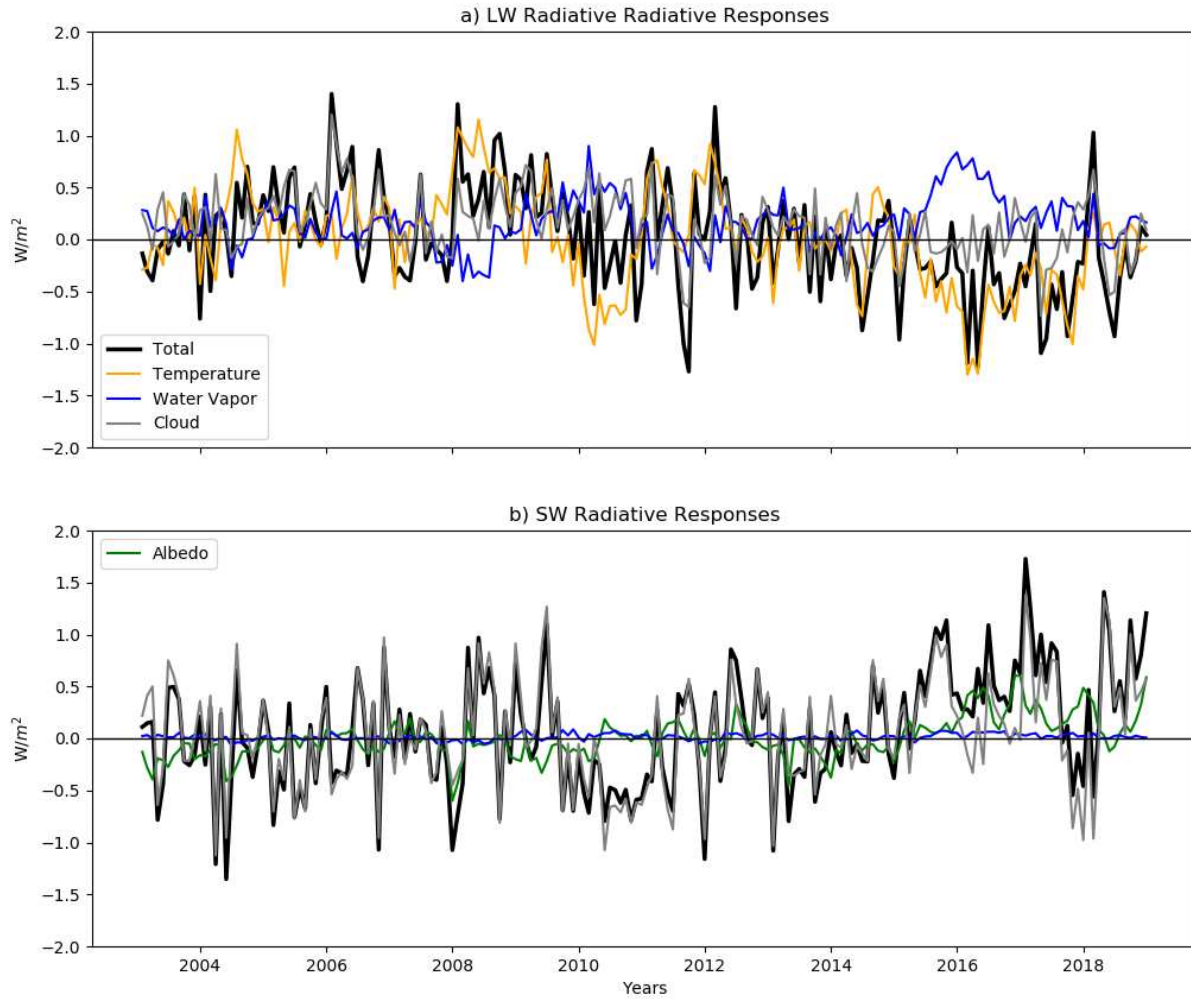
871
872



873

874 **Figure S3.** Global-mean total radiative flux anomalies (black) as measured by CERES and the
875 contribution from radiative feedback processes (red). Both quantities are smoothed with a 12-
876 month moving average. The Niño3.4 Index (NOAA/NCEP CPC) is overlaid (blue dashed).

877
878
879
880

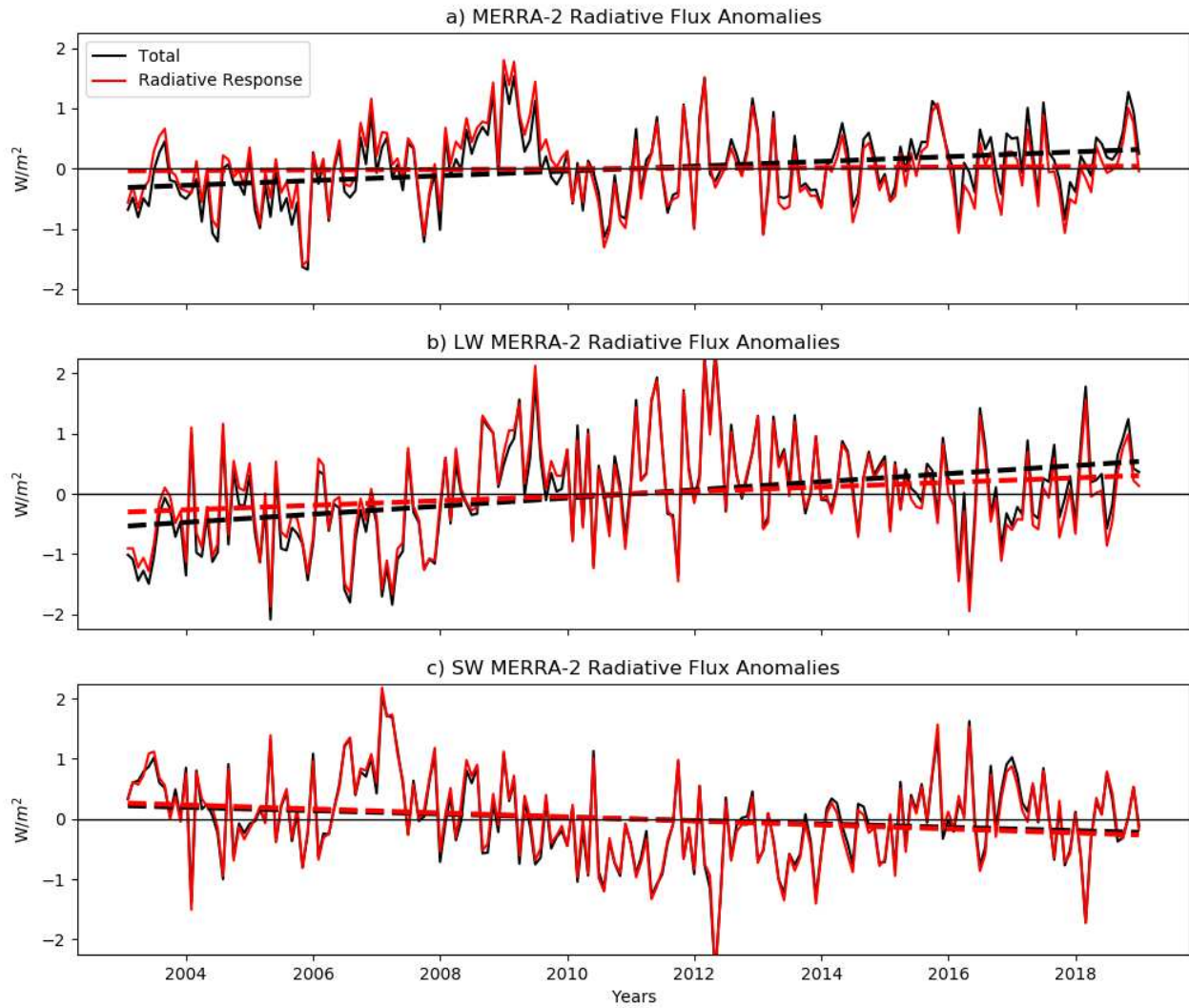


881

882 **Figure S2.** The total a) longwave (LW) and b) shortwave (SW) radiative response and its

883 decomposition into individual radiative responses in CERES/AIRS observations.

884



885

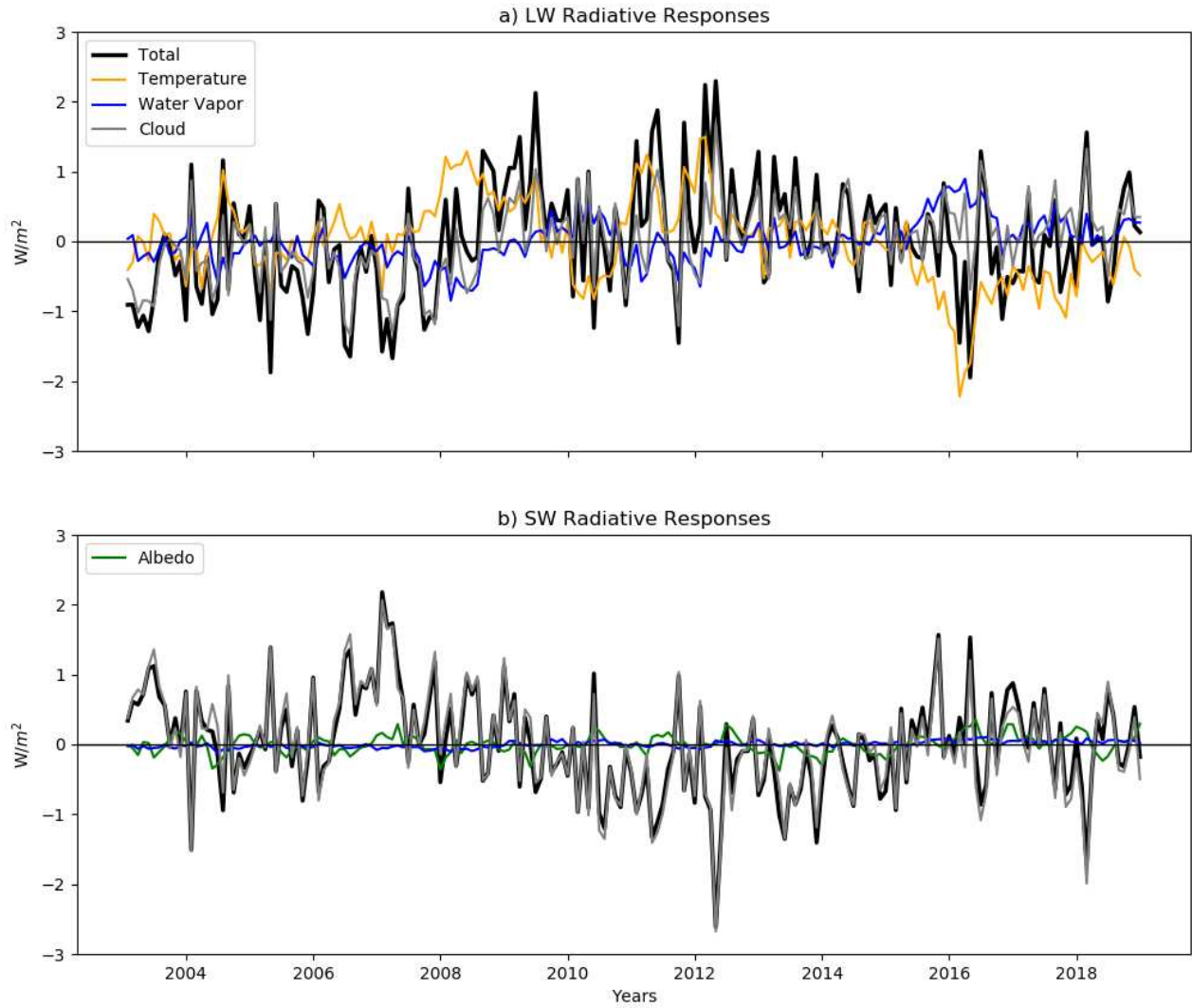
886 **Figure S3.** Global-mean, MERRA-2 a) net, b) longwave (LW) and c) shortwave (SW) total

887 radiative flux anomalies (black) from 2003 through 2018 and the contribution to that total from

888 the sum of radiative responses (red). Respective trendlines are displayed as dashed lines.

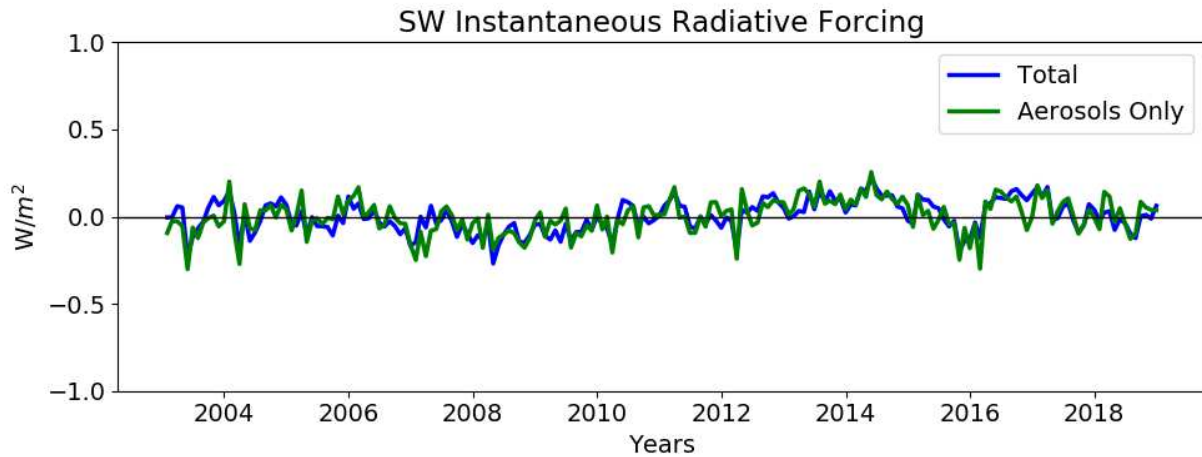
889

890



891
892
893

Figure S4. Same as Figure S2 but for MERRA-2.

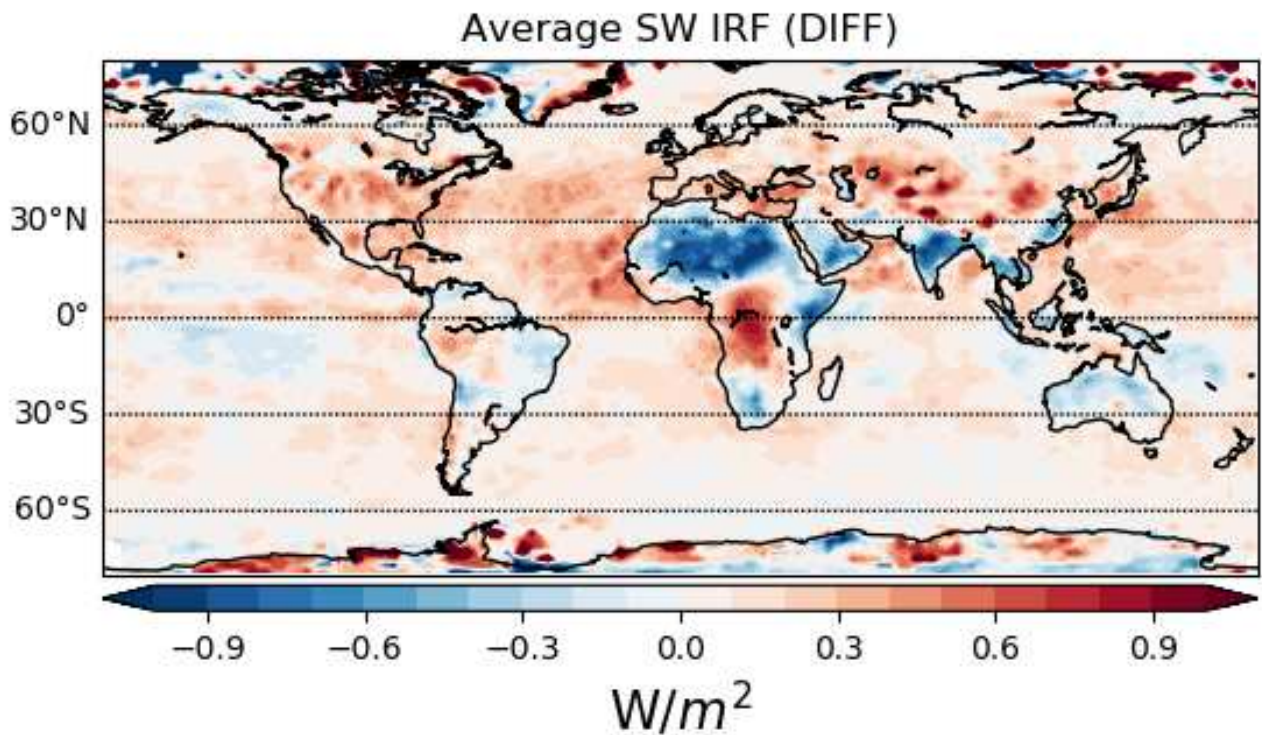


894

895 **Figure S5.** Global-mean a) total shortwave instantaneous radiative forcing (SW IRF) from
 896 MERRA-2 derived from the kernel differencing technique and b) aerosol-only SW IRF from
 897 direct output of MERRA-2 radiative flux diagnostics.

898

899

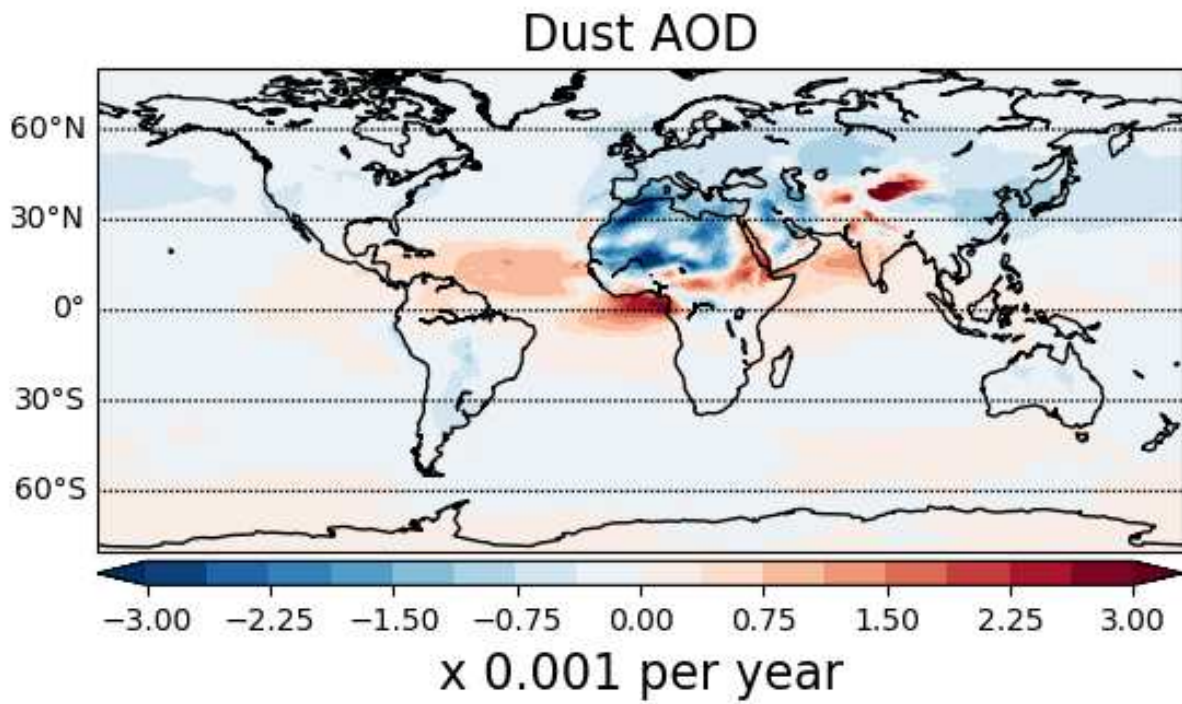


900

901 **Figure S6.** Average difference (CERES/AIRS minus MERRA-2) in SW IRF from 2016 through

902 2018.

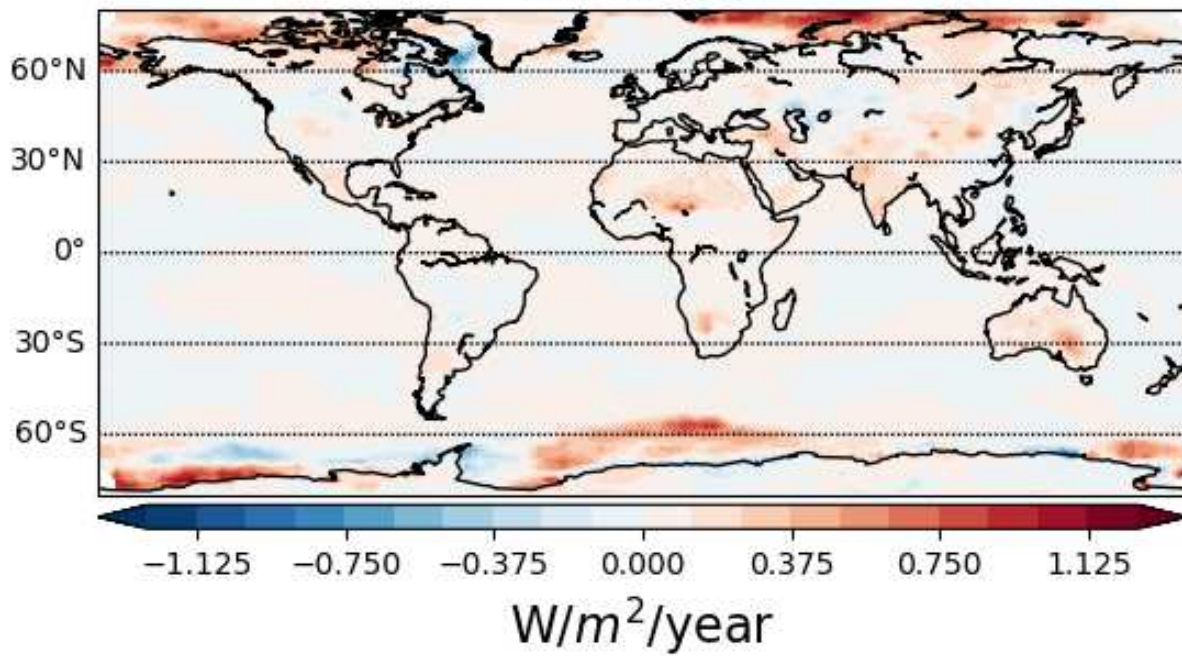
903
904
905
906



907
908 **Figure S7.** Local linear trends from 2003 through 2018 in dust aerosol optical depth from
909 MERRA-2 reanalysis.

910
911
912
913

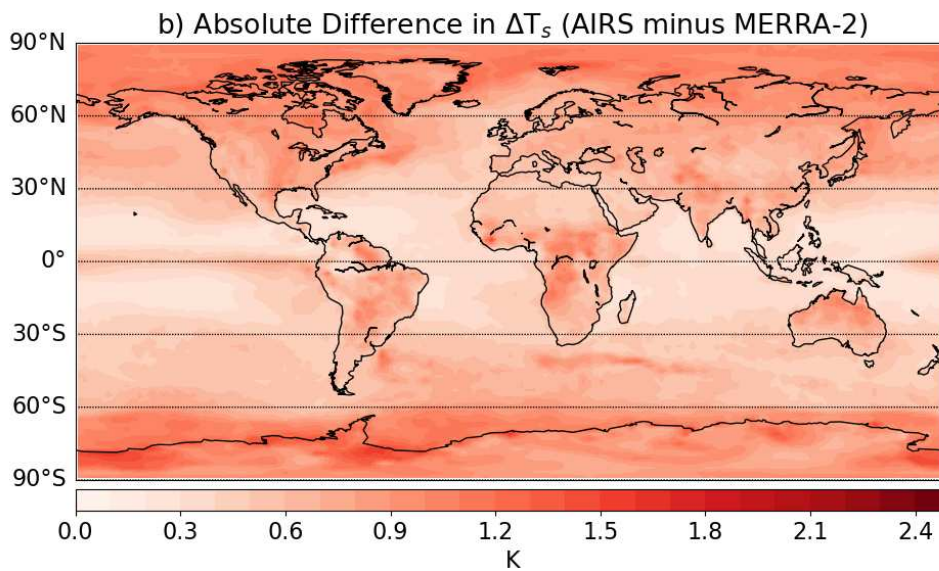
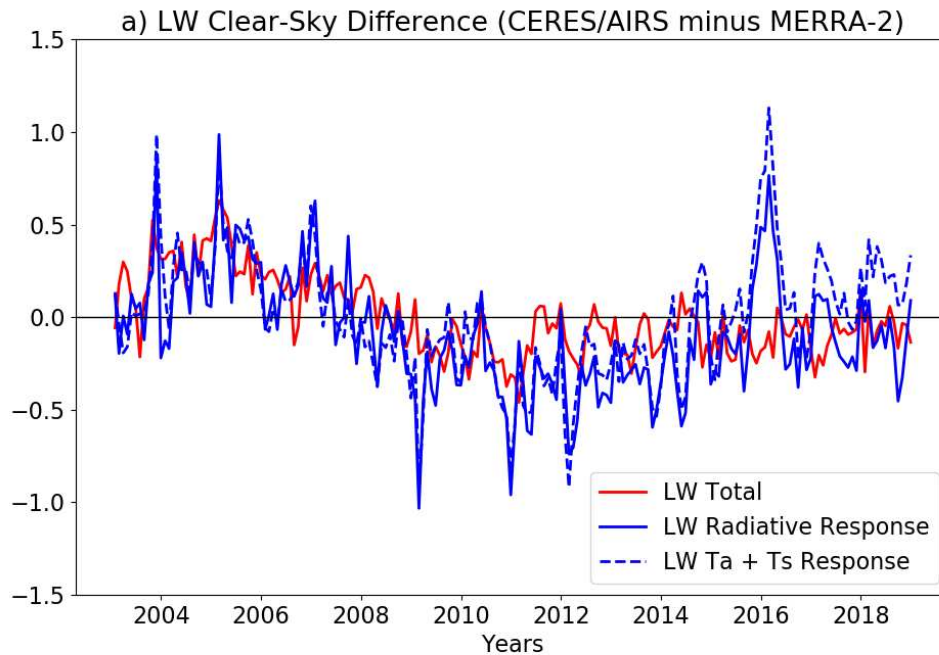
914



915

916 **Figure S8.** Local linear trends from 2003 through 2018 in clear-sky surface albedo radiative
917 response, used in the kernel differencing method to derive shortwave instantaneous radiative
918 forcing (SW IRF).

919

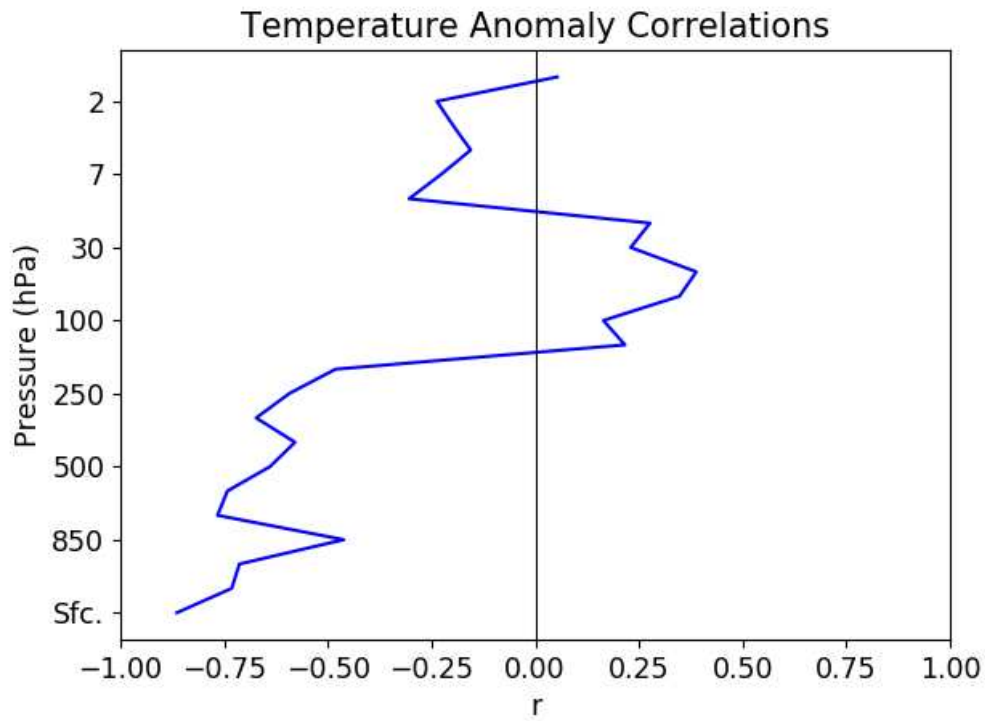


920

921 **Figure S9.** a) Difference between satellite observations and MERRA-2 in global-mean longwave
 922 (LW) total radiative flux anomalies (red solid line) as well as the contributions from the sum of
 923 LW radiative responses (blue solid) and the LW temperature radiative response (blue dashed), in
 924 isolation. b) Mean absolute difference between satellite observations and MERRA-2 in local
 925 surface temperature anomalies.

926

927



928

929 **Figure S10.** Correlation of the global-mean differences in the temperature feedback between
930 CERES/AIRS and MERRA-2 with differences in temperature anomalies at each vertical level
931 and the surface.

932

933

934

935

936

937

938

939

940

941

942

943

944

945

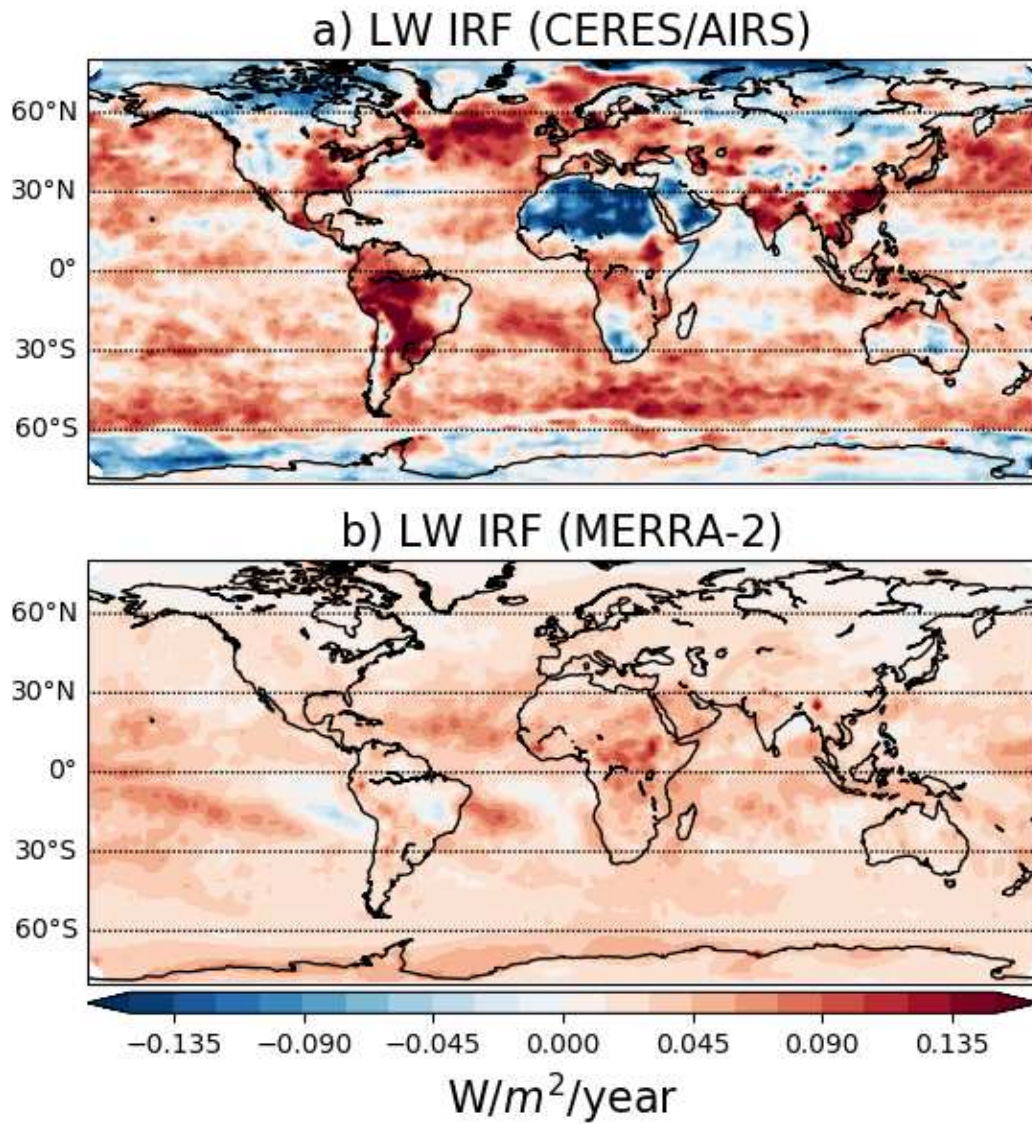


Figure S11. Local linear trends from 2003 through 2018 in all-sky longwave instantaneous radiative forcing (LW IRF) diagnosed in a) CERES/AIRS observations and b) MERRA-2 reanalysis.